The Pennsylvania State University
The Graduate School

PASSIVE TRAILING EDGE NOISE ATTENUATION WITH POROSITY, INSPIRED BY OWL PLUMAGE

A Thesis in
Bioengineering
by
Zachary W. Yoas

Submitted in Partial Fulfillment
of the Requirements
for the Degree of

Master of Science

August 2021

The thesis of Zachary W. Yoas was reviewed and approved by the following:

Michael H. Krane
Associate Research Professor of Fluids Research
Thesis Advisor

Adam S. Nickels
Research and Development Engineer of Fluids Research

William Hancock
Professor of Biomedical Engineering

Daniel Hayes
Professor of Biomedical Engineering and Graduate Programs Coordinator

Abstract

The quiet flight of large owl species has been attributed to their porous plumage of their wings. Specifically, the wing porosity modifies the sound produced by the interaction of eddies in the turbulent boundary with the trailing edge of their non-compact trailing wings. Theoretical predictions have demonstrated that this porosity changes both the radiated sound levels and directivity. Moreover, the radiated sound depends on open area α and porosity diameter R, relative to acoustic wavenumber k, through the nondimensional parameter μ/k, where $\mu = \alpha/R$. These predictions have proved difficult to validate in wind tunnels because as porosity increases, the trailing edge noise source decreases in amplitude, relative to other sources of sound in the tunnel. The current study addresses this issue by a) reducing the problem to its fundamental element, the sound produced by the convection of a single vortical eddy past the edge of a non-compact surface, and b) by removing all other flow features by utilizing an anechoic chamber to collect measurements. This approach has been shown to be effective for validating the theoretical sound power scaling laws for a vortex ring convecting past the edge of an impermeable large flat plate.

Measurements of the sound produced by this interaction were performed in the ARL Penn State anechoic chamber for a series of plates, each with a different porosity, where the control case being a rigid, impermeable plate. The vortex rings, produced by a shock tube, developed from a 6mm diameter nozzle. Vortex ring motion and size were estimated from high speed Schleiren imaging of the vortex ring motion, captured at 25.1 kHz. Ring speed ranged from 39 m/s to 86 m/s, while the ring radius was 6.5 mm when the vortex ring was directly above the edge. Twelve microphones, arranged in a circle centered on the plate edge, were used to measure farfield sound pressure and directivity. These measurements were used to estimate the exponent in the sound power $\sim U^n$ and $\sim L^m$ scaling laws. Predicted changes in n, m, farfield sound directivity, and source waveforms for increasing porosity show favorable comparisons to measurement.

Contents

List of Figures

List of Tables

List of Symbols

a	Radius of vortex ring
$\beta(\theta)$	Radiated noise directivity
c_o	Speed of sound
δ_{ij}	Kronecker delta
D_i	Source waveform at angle θ
D_{avg}	Average source waveform
f_s	Source frequency
H	Nozzle diameter
k	Acoustic wave number
l	Characteristic length scale of source interaction
L	Impact distance, i.e. offset between vortex ring and plate edge
λ	Source acoustic wavelength
m_i	Impact distance scaling exponent at angle θ
$\bar{m}$	Average impact distance scaling exponent
M	Mach number
n_i	Sound power power law exponent derived from measurements of a microphone at angle θ_i
$\bar{n}$	Average sound power power-law exponent derived from measurements

ρ_o Fluid density

ρ' Density fluctuations due to acoustic disturbance

p' Pressure fluctuations due to acoustic disturbance

p_i Farfield pressure at angle θ

Re Reynolds number

σ_{ij} Friction stress

TE Lifting surface trailing edge

t_s Source interaction time of vortex ring and plate edge

u_o Fluid velocity

u' Fluid particle velocity fluctuation due to acoustic disturbance

U_R Vortex ring characteristic speed

μ Fluid dynamic viscosity

ω Angular frequency of source

VR Vortex ring

VRG Vortex ring generator

Z_p Horizontal offset distance, normal to plate, between the nozzle and plate edge

Acknowledgments

Foremost, I am very grateful and fortunate for the support and guidance from my adviser, and dear friend, Dr. Michael Krane. His willingness to share his time, experience, and instruction to ensure my professional development has been invaluable. I would like to thank my previous mentors Dr. Timothy Brungart and Brian Kline for a) the memorable years of working together and b) their advice and encouragement continue my education. A special acknowledgement to Dr. Kofi Adu for introducing me to research, and shaping my thought process for problem solving. I would like to thank my committee members Dr. William Hancock and Dr. Adam Nickels for their oversight of my thesis and program. To our collaborators Dr. Justin Jaworski and Huansheng Chen from Lehigh University, I am very appreciative of the contributions, comments, and insight into the theoretical aspects of the experiment. Much of this would not have been possible without you. To my fellow friends and colleagues at the Garfield Thomas Water Tunnel Building, thank you for the continued support that you have given over the many years prior to & during my master's program. I am grateful for the financial support received from the National Science Foundation (NSF CBET-180445) and the Applied Research Laboratory, making this possible. Finally, I would like to thank my friends, family, and loved ones for supporting me – specifically, my dear friends Dr. Gage Walters & Paul Trzcinski.

Any opinions, findings, and conclusions or recommendations expressed in this material are those of the author and do not necessarily reflect the views of the National Science Foundation.

Chapter 1

Introduction

1.1 Problem Statement

As an object moves through the air it can produce undesirable noise that originates from the unsteady force exchange between the fluid and structure. The sound generating pathways include sources from a) structural vibrations and b) turbulence interacting with the body. The scope of this paper investigates a specific subset of turbulence interacting with a body known as trailing edge (TE) noise, defined as the noise generated by eddies from the turbulent boundary layer convecting past a lifting surface's TE. This noise source, which has been shown by Ffowcs-Williams and Hall [2] to dominate over other aero-acoustic sources at low Mach number (M) flows, is observable in scenarios like airframe noise, particularly upon landing approach, wind turbine blades, and avian flight. Figure 1.1 illustrates this process.

Here, a stationary rigid impermeable airfoil is immersed in a boundless fluid medium moving left to right at speed U. Viscous effects induce a boundary layer formation (δ) along the body. When sufficient chord length is available, this layer becomes turbulent. This layer is composed of many vortical eddies that vary in strength and size. As these vortical structures convect past the sharp TE on either side of the airfoil they produce a force normal to the edge that results in radiated sound. The simultaneous convection of many large and small eddies past the edge produce the perceived broadband noise signature.

For aircraft, reducing trailing edge noise has become more important as jet engine noise has been steadily reduced. [3] Other lifting surface applications where excessive TE noise has been addressed include wind turbines, cooling fans, and UAV propulsions. [4;5;6] In an effort to reduce aural detection, the defense sector has allocated considerable funds to attenuate the

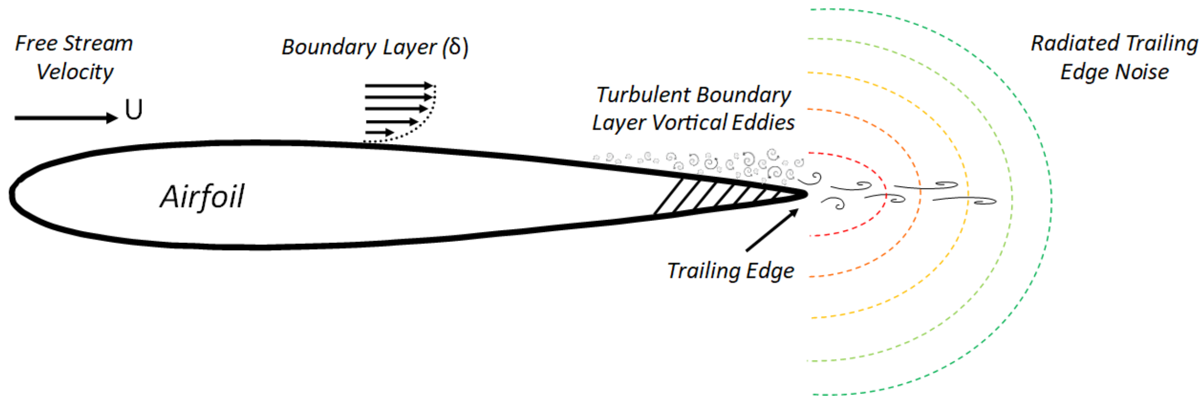

Figure 1.1: Schematic of the turbulent boundary, formed on a single side of the airfoil for clarity, and trailing edge noise

acoustic signature of drones, gliders, and aircraft. In a similar fashion, wind-turbine farms have been federally regulated to reduce the intense low frequency sound produced by the TE noise of the large sharp blades, Arnett et. al.[7]. Ordinances regulating noise, motivated by concerns regarding environmental damage, Arnett et al.[7], and community annoyance, Bolin et al.[8], have set allowable noise limits. To remain compliant wind-turbine farms have since altered operations by implementing rotor braking, adjusting the blade angle of attack, and modifying TE designs. While these solutions help mitigate the undesirable TE noise they also lead to reduced performance. Therefore, companies invest funds to further research methods for TE noise control.

For rigid impermeable airfoil types, i.e. aircraft airfoils, wind-turbines, etc, Ffowcs-Williams and Hall[2] identified the sound generated by the TE to scale as $\Pi_{rp} \sim U^3(\frac{U^2}{c^2}) \sim U^3M^2 \sim U^5$ for low Mach number flows. Here Π_{rp} represents radiated sound power, c the speed of sound, and M the Mach number. Since M is much less than 1 for these conditions, it is clear how the TE sound generation would a) increase as the exponent of U^n decreases, or b) decrease as the exponent n increases. Ffowcs-Williams and Hall[2] also identified criteria for TE noise to occur as a function of eddy/edge offset distance – i.e. at what distance from the edge does the plate start to baffle the noise source and the noise generation increases. When the offset distance between the edge and center of the eddy, L, is large the plate amplification effects diminish. Specifically, when $(kL)^{1/2} \gg 1$, where k is the acoustic wave number, the radiated sound power scales as U^8. This condition is similar to an eddy convecting in free space, which is discussed later in Chapter 2.4. When L is small, i.e. the eddy is close to the edge, and $2kL \ll 1$, the noise radiation increases to $\Pi_{rp} \sim U^5$. In addition to the sound power scaling with eddy speed, U, Ffowcs-Williams and Hall[2] predicted acoustic directivity to be cardioid, in the form $\sin^2(\theta/2)$, from the eddy/edge interaction. This was later supported by theoretical efforts that include Hayden[9], Goldstein[10], and Kambe et al.[11].

Empirical support for Ffowcs-Willams and Hall's U^5 scaling came from Fink[12] who tested an airfoil in an anechoic wind tunnel. Measurements were collected from a) flow over a single side of a wing and b) flow on both sides of a wing. Additional experimental confirmations for U^5 include Brooks and Hodgson[13], Kambe et al.[11], Oerleman and Migliore[14], Geyer et al.[15], and Herr et al.[16]. Kambe et al.[11] recast the TE problem to its essence, as a single eddy, in the form of a vortex ring, passing near the edge of a half plane where all time scales where determined by the motion of the vortex ring. Their tests assessed sound power scaling with both ring speed, U, & impact distance, L, and addressed acoustic directivity for the vortex ring / edge interaction. Their results showed sound power to scale as $\Pi_{rp} \sim U^5 L^{-4}$, and radiate sound from the vortex ring / edge interaction to take a cardioid directivity pattern, as predicted by Ffowcs-Williams and Hall[2].

In an effort to passively suppress TE noise, methods have drawn inspiration from the quiet flight of large owl species. Graham[17] suggested that one mechanism for owl quiet flight be attributed to their porous and compliant TE feathers. Kroeger et al.[18] quantified Graham's observations with owl fly over experiments and identified the large owl species generate low frequency sound, which was claimed to be associated to an evolutionary advantage over their prey, who's hearing has a lower sensitivity at these lower frequencies. Klan et al.[19] and Bachmann et al.[20] expanded upon Kroeger et al.[18] and both found the downy coating on the owl wing allows for the flow to remain attached to the wing, allowing for slower flight speed which reduces noise levels and source frequency. Further evidence from Lilley[21] suggested the thin diameter feathered fringe along the TE dampens the vortical eddies convecting near the TE for frequencies approximately above 2kHz. Sarradj and Geyer[22] and Geyer et al.[15;23;24], through a series of fly over and wind tunnel testing demonstrated the poro-elastic features of owl wing anatomy reduce noise levels, compared to similar geometry impermeable airfoils and other avian species. Clark[25] and Clark et al.[26;27] performed similar wind tunnel experiments and observed up to $\simeq 10dB$ reductions in radiated sound from TE treatments that mimic owl morphology. The aforementioned studies presented experimental evidence that demonstrated TE bio-mimicry lead to decreases in noise levels.

However, one shortcoming of their work was the lack of theory to predict sound levels at the design stage – a critical requirement.

Predictions of radiated noise from porous lifting surfaces were considered by Leppington[28;29] and Howe[30;31]. Their theoretical work demonstrated reductions in TE radiated noise with even spaced apertures, which increased the acoustic transparency of the plate. This effectively removes the baffling surface of the impermeable plate. Their results identified the radiated sound power to scale as $\Pi_{rp} \sim U^6$ with a dipole directivity as $sin^2(\theta)$. Khorrami and Choudhari[32] later numerically investigated the effects of porous treatments with time-accurate simulations on Reynolds averaged Navier Stokes equations, and demonstrated porous treatments lead to ~20 dB decreases in radiated noise. Jaworski and Peake[33] then introduced a theory that related TE sound generation from porous, elastic, and poro-elastic edge types – inspired largely by the silent flight of owl species. (This work focuses solely on the effect of plate porosity). Their theoretical predictions, which employed a Weiner-Hopf technique to solve the TE noise problem, identified parametric limits where reductions in TE noise scaled as $\Pi_{rp} \sim U^6$. This scaling is achieved when a set of criteria, mentioned in Equation 1.1, are met, where $\bar{K_R}$ is Rayleigh Conductivity, $\alpha = N\pi R^2$, N the number of apertures of hole radius R divided by the plate area, and k as $2\pi f_s/c$, where f_s is the frequency of the source. The expression μ/k, where $\mu = \alpha_H \bar{K_R}/R$ will be used for the rest of this document. For high μ/k, it is shown the effect of porosity to reduce the radiated noise is a function of R and k. This means as the acoustic transparency of plate increases, the nearfield baffling from the plate is progressively relieved.

$$\Pi_{rp} \sim \begin{cases} U^3 M^2, & \frac{\alpha_H \overline{K}_R}{(kR)} \ll 1 \\ (\frac{\alpha_H}{R})^{-1} U^3 M^3, & \frac{\alpha_H \overline{K}_R}{(kR)} \gg 1 \end{cases} \tag{1.1}$$

Cavaleri et al.[34] extended Jaworski and Peake's[33] approach with consideration of finite-chord poroelastic edge geometries; a more practical airfoil design. These numerical results showed U^6 scaling behavior for porous plate configurations when Ω = 0.04-0.25, where $\Omega = k/k_B$ and k_B is the bending wave number. Furthermore, these results indicated porosity to effectively reduce radiated noise when $k_0 \ll 1$. The distribution and localization of porosity on the lifting surface was assessed by Zhou et al.[35] with a discrete adjoin approach, where the control theory is applied a set of discrete field equations. This result demonstrated noise reductions of $\sim 9dB$ above uniform porous distributions. Kisil and Ayton[36] numerically studied the effects of porous appendages along the TE of an impermeable plate and showed its effectiveness to reduce TE noise. Inspired by the approach Kambe et al.[11], Chen et al.[1] investigated the sound radiation from a vortex ring passing near the edge of a porous plate. A schematic of this approach is shown in Figure 1.2. Chen et al.[1] showed sound power scaling, when $\mu/k \gg 1$, as $U^6 L^{-5}$. Furthermore, their results show the change in behavior of source waveforms and directivity as the μ/k transitions from a) rigid impermeable to b) rigid and highly porous conditions. As the plate transitions from a) to b) it was shown the directivity transitions from cardioid as $sin^2(\theta/2)$ to dipole as $sin^2(\theta)$, respectively.

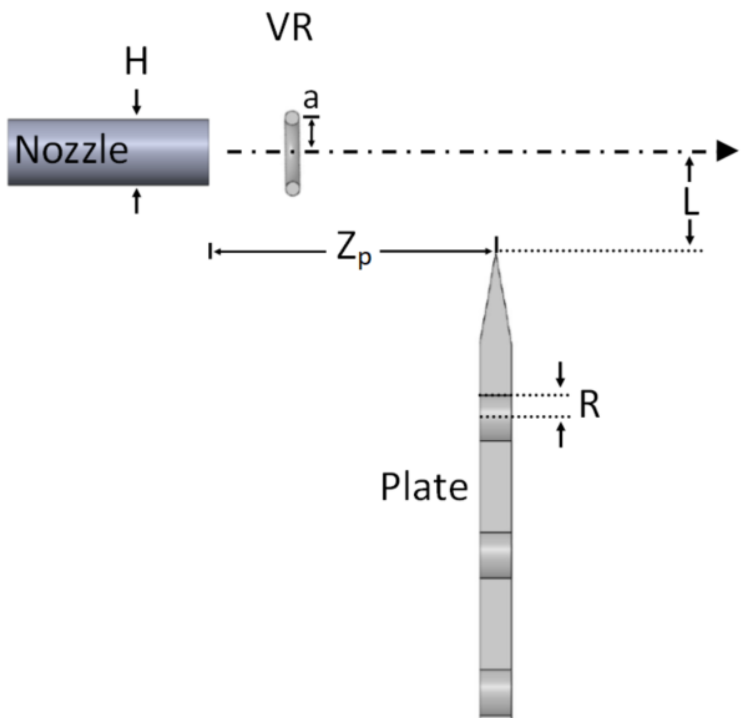

Figure 1.2: Trailing edge noise problem modeled as a vortex ring passing near an edge of a porous plate. Here, H is the nozzle diameter, L impact distance, Z_p offset between the nozzle and edge, a vortex ring radius, R the radius of the hole, and VR the vortex ring convecting at speed U.

To the best of the author's knowledge, empirical evidence that supports the sound power scaling laws proposed by Jaworski and Peake[33] and Chen et al.[1] remain elusive.

1.2 Summary of Contributions

Porous treatments to lifting surfaces have been shown to reduce TE noise, as shown in Chapter 1.1. While predicted sound power scaling laws [33;34;1] have been made, empirical verification remains lacking. This is largely due to the excessive background noise inherent to wind tunnels overwhelming the TE noise that diminishes with porosity. The purpose of the presented work seeks validate the sound power predictions by modeling the problem similar to Kambe et al. [11], where measurements were acquired in anechoic chamber from a single eddy, in the form of a vortex ring, passing near a plate edge. With this approach a) the relationship between the vortex motion and frequency of the radiated sound is clear, and b) the radiated noise is not competing with other noise sources present in a wind tunnel. Validation will be achieved in the following ways:

1. Determine the radiated sound scaling as a function of vortex ring characteristic speed, U_R, for increasing acoustically transparent plates

2. Investigate the radiated sound scaling as function of impact distance, L, for both the rigid impermeable and highly acoustically transparent plates

3. Determine the radiated sound directivity pattern as the near-field transparency of the plate increases

4. Compute and compare the experimental and theoretically predicted source waveforms with increasing porosity

The principle contribution of this effort will be to validate the theoretical predictions to reduce trailing edge noise with porosity.

Chapter 2

Background

2.1 Overview

The objective of this chapter is to introduce and define the concepts and definitions necessary to understand the aero-acoustic theory associated with the vortex/edge experiment. Key concepts include acoustic sources and acoustic compactness. Sound radiation for the following cases will be discussed for vortex fluid motion convecting a) in *free space*, b) near a *compact body*, and c) near a *non-compact body*. The latter condition will be expanded to include vortex fluid motion convecting near the edge of non-compact a)*rigid impermeable body*, and b)*rigid permeable body*.

2.2 Acoustic Sources

An aero-acoustic source can be modeled as a single or multiple combination of monopoles, dipoles, and quadrupoles. For this discussion it is assumed the source is fixed in space and the only motion is due to rarefaction and compression. A monopole noise source, represented in Figure 2.1 a), will expand and contract periodically causing pressure fluctuations that propagate away from the source. In free space this pulsing source will radiate sound evenly in all directions. This acoustic directivity is known as omnidirectional.

Dipoles are composed of two monopoles, 180° out of phase, and separated by a distance of less than a wavelength. This condition is shown in Figure 2.1 b). Here it is observed the acoustic directivity transitions from spherical to a distinct double lobed dipole. To

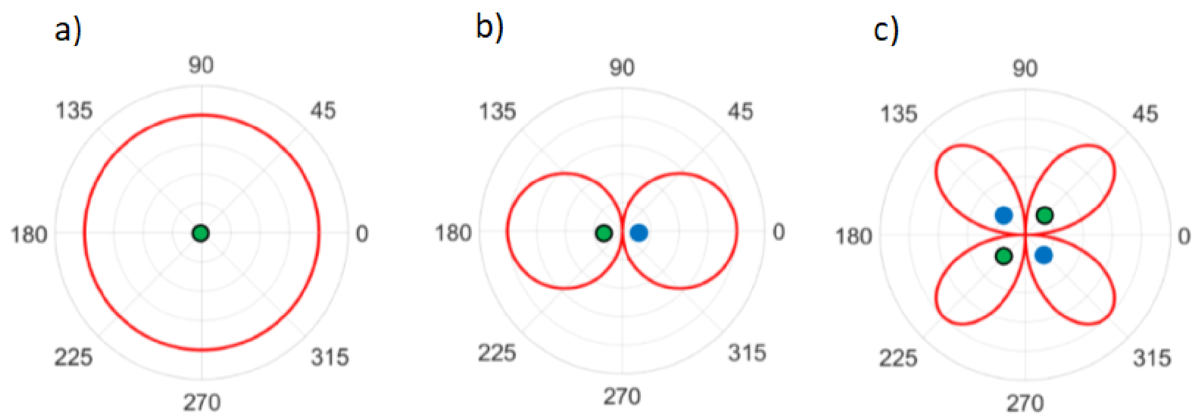

Figure 2.1: Radiated sound directivity, shown as a (–), for a) monopole , b) dipole, and c) quadrupole sources.

understand why this transition occurs, an understanding of the acoustic nearfield is necessary. As the two spheres expand and contract they impart a force on the local fluid. In between the spheres the fluid motion is sloshed, due to the 180° difference, where energy that once propagated into the farfield, in the case of the monopole, is inhibited. This constrained energy is therefore responsible for the characteristic double null of the dipole. While dipoles are less efficient radiators of sound, compared to monopoles, their nearfield strength is much more significant. When two dipoles are placed within a wavelength of one another, as shown in Figure 2.1 c), they form what is known as a quadrupole. As with the dipole, the close proximity of these sources leads to an increased constrained energy within the nearfield – energy that would typically be release as sound. Because of this, the quadrupole, in this configuration, forms two additional lobes for the same reason mentioned in the dipole case. Again, it is significant to note this constrained energy a) reduces the farfield radiated noise produced by a quadrupole and b) increases the nearfield strength. When bodies are introduced into the nearfield for cases b) and c), they can act as baffles which allow for this energy to be released. The size of these bodies and their impact on the radiated noise will be addressed in the next sections.

2.3 Compactness

As the radial distance from the center of the source increases the behavior of the radiated noise changes. This condition, which separates the far and near fields, is known as compactness. The compactness condition is defined by the non-dimensional parameter ka, where k the acoustic wave number defined as $k = \omega/c$ and a the characteristic dimension of the source. For $ka \ll 1$, i.e. the sphere is smaller than a wavelength of sound, the source is considered *compact* and can be treated as a simple source or point source. Alternatively when $ka \gg 1$, i.e. a high vibration frequency or the sphere is large, the source is considered *non-compact*.

To determine if the compactness condition applies to the vortex edge experiment, characteristics of the flow field and structure must be defined. The convection velocity is defined as U_R, speed of sound c, Mach number $M = U_R/c$, and characteristic length l. The source interaction time is defined as $t_s = l/U$ and source frequency $f_s = (1/t_s)$ or $f_s = U/l$. The wavelength of the source would therefore be $\lambda = l/M$. When the wavelength of the source, λ, is larger than the characteristic length of the body, this condition is defined as compact. For the vortex / plate experiment the source region containing the vortex ring and edge is smaller than a wavelength, so it is considered compact. However, while this source is compact, it may also be in the presence of a non-compact body, i.e. the plate, which affects sound radiation from the source.

2.4 Aeroacoustic Theory

The study of aero-acoustics focuses on sound generated by unsteady fluid flows. Analyzing flow fields and noise emanating from airfoils, jets, or human voice are a few applications of aero-acoustic studies.[13;37;38] In an effort to attenuate airfoil noise, a great deal of research has been devoted to the study of the trailing edge noise radiation mechanism.

As an object moves through a fluid, the formation of a boundary layer occurs as a result of the velocity gradient between the free stream and zero-velocity, due to the no-slip condition, of the fluid adjacent to the body's surface. This boundary layer is characterized as either laminar or turbulent based upon the calculated Reynolds number, $Re = \rho U_R l/\mu$, where Re is the Reynolds Number, ρ the fluid density, U the free stream velocity, l characteristic length scale, and μ the dynamic viscosity. This nondimensional parameter Re indicates whether inertial or viscous effects dominate the system. High Reynolds numbers are dominated by inertial effects and indicate turbulent boundary layer formation, whereas low Reynolds numbers are viscous dominated and form a laminar boundary layer. For TE noise in this paper, a turbulent boundary layer is assumed. Figure 1.1 illustrates this type of scenario.

2.4.1 Radiated Noise From Turbulent Fluid Motion

In 1952 Lighthill[39] pioneered the field of aeroacoustics with a theory that united fluids and acoustics so that noise radiation from turbulence in free-space could be predicted. This was achieved by modification of the right hand side of the inhomogeneous continuity and momentum equations, shown in equations, 2.1 and 2.2 respectively. Here, p' and ρ' are written in terms of acoustic fluctuations, which assume the small signal approximation where acoustic fluctuations are minute relative to the quiescent ambient fluid.

$$\frac{\partial \rho'}{\partial t} + \frac{\partial \rho' u_j}{\partial x_j} = q \tag{2.1}$$

$$\frac{\partial \rho' u_i}{\partial t} + \frac{\partial \rho' u_i u_j}{\partial x_j} = -\frac{\partial p'}{\partial x_i} + f_i + \rho' g \tag{2.2}$$

The right hand side of Equation 2.1, q, accounts for the injection of mass. Similarly for Equation 2.2 the source terms are p' the stress tensor which represents stress due to pressure and viscous shear stress, f_i externally applied forces, and $\rho' g$ the gravitational forces, which will ignored. By taking the divergence of the momentum equation, then subtracting the time derivative of the continuity equation, and introducing the isentropic relationship between acoustic pressure and density, the equation of state, the inhomogenous wave equation takes form.

$$\frac{\partial^2 \rho'}{\partial t^2} - c_o^2 \frac{\partial \rho'}{\partial x_i \partial x_i} = \frac{\partial^2 \tau_{ij}}{\partial x_i \partial x_j} \tag{2.3}$$

where τ_{ij} represents the Lighthill's stress tensor defined in Equation 2.4.

$$\tau_{ij} = \rho u_i u_j - \sigma_{ij} + (p - c_o^2 \rho)\delta_{ij} \tag{2.4}$$

Here, $\rho u_i u_j$ is the turbulent stress, σ_{ij} the sound created by viscosity, and $(p - c^2{}_o \rho)\delta_{ij}$ processes in the source regions for which the relationship between pressure and density is non-isentropic, where δ_{ij} is the Kronecker delta function. Lighthill identified noise radiation from a turbulent eddy in a boundless medium to scale as $\Pi_{rp} \sim U^3 M^5$, or U^8.

Powell[40] attributed the radiated noise in turbulent flow to the flow vorticity. This framework lead to Mohring[41] and Obermeier[42] to identify the linear relationship between the vorticity and sound. These theoretical results that build upon Lighthill[39], where sound arose from $\rho u_i u_j$ as the source, could be written in terms of vorticity, which could be further described as vorticity impulse. This allowed for the turbulent eddy, modeled as a vortex ring, to be replaced acoustically as a dipole associated to the vortex impulse, and also a quadrupole. A schematic of the source modeled as a vortex ring is shown in Figure 2.2 A). Kambe et al.[43] expanded on Mohring and Obermeier's[41;42] findings to theoretically show the emitted acoustic wave is related to the system of compact vortices. The theoretical emphasis on vorticity was later confirmed experimentally in Kambe et al.[44] with the collision of two vortex rings.

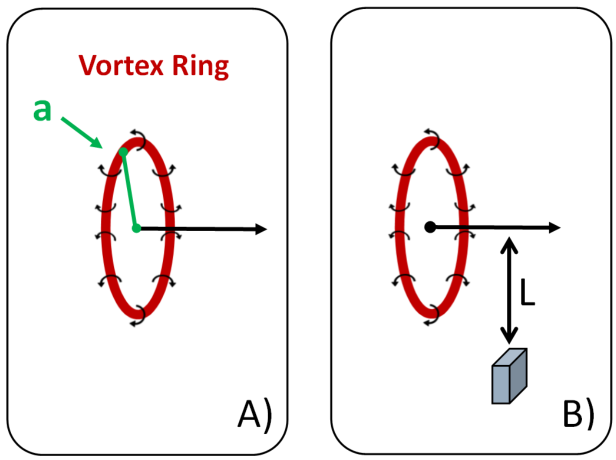

Figure 2.2: Schematic of compact acoustic source, in the form of a vortex ring A) convecting in free space and B) near a compact body

2.4.2 Radiated Noise From Turbulent Fluid Motion Interacting With Surfaces

2.4.2.1 Turbulence Interacting With Compact Bodies

Curle[45] developed a theoretical description for turbulence interacting with compact solid bodies. This method, shown in Figure 2.2 B) where he accounted for stress on the solid body surface and surface motions as the sources of sound. From each source term he identified the source type, i.e. monopole, dipole, quadrupole, and related it to the source term. When a compact solid body is present, the dipole component dominates the other sources leading to $\Pi_{rp} \sim U^6$ scaling.

2.4.2.2 Turbulence Interacting With Non-Compact Rigid Impermeable Plate

Since the theoretical predictions and experimental findings for this condition have largely been discussed in Chapter 1 a brief overview will be presented here. Theoretical predictions for aerodynamic noise generated by turbulent fluid motion interacting with a non-compact body were first made by Ffowcs-Williams and Hall[2]. This condition is observed in Figure 2.3 a). Here, as mentioned in Chapter 1, the sound power scales as U^5L^{-4}. Furthermore, it has been shown in the aforementioned section that the acoustic directivity for this condition is in the form of a $sin^2(\theta/2)$ or cardioid. This radiation directivity is shown in Figure 2.4. The amplification of the noise from the vortex passing near the non-compact rigid plate arises from the rigid impermeable plate baffling the near field of the edge dipole.

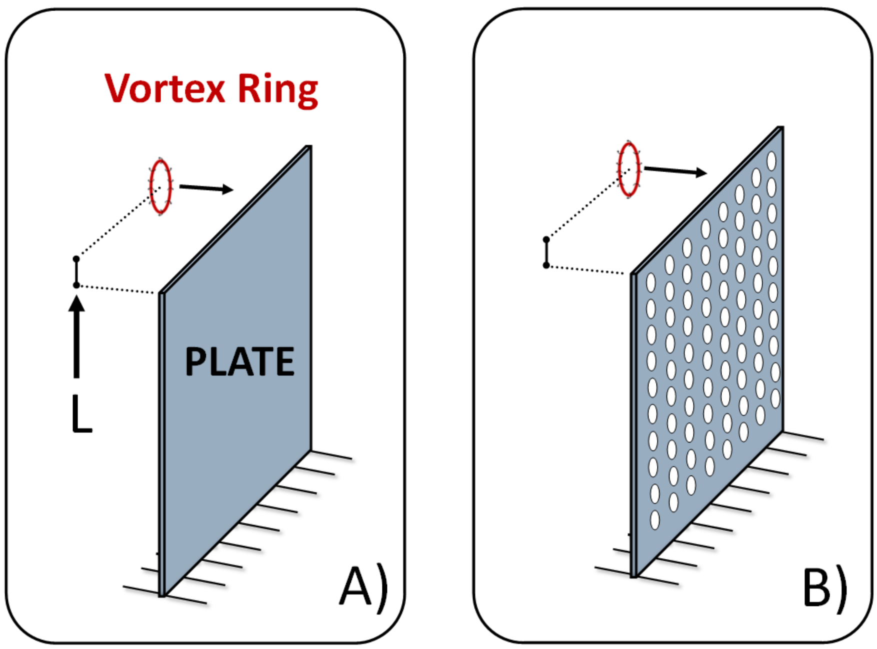

Figure 2.3: Schematic of a compact acoustic source, in the form of a vortex ring convecting near a A) rigid impermeable plate and B) non-compact rigid porous plate.

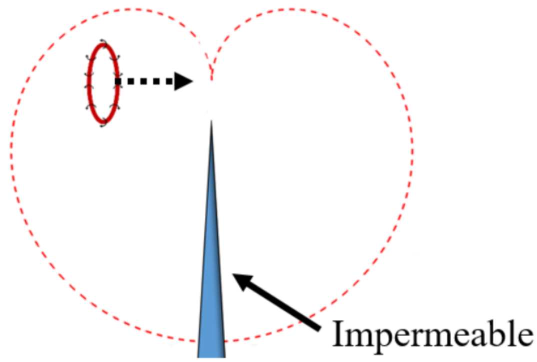

Figure 2.4: Cardioid sound directivity from a vortex ring convecting near an impermeable non-compact plate

2.4.2.3 Turbulence Interacting With Non-Compact Rigid Porous Plate

Again, since this condition was expanded upon in Chapter 1 this section will remain brief. For a non-compact rigid porous plate the theoretical sound power scaling has been shown to scale as U^6[33]. A schematic of this condition is shown in Figure 2.3 B). This reduction in radiated noise is achieved by the increase acoustic transparency, as shown in Figure 2.5. Jaworski and Peake[33] identified μ/k as the parameter of interest that determines the sound power scaling, n, as it transitions from U^{5-6}.

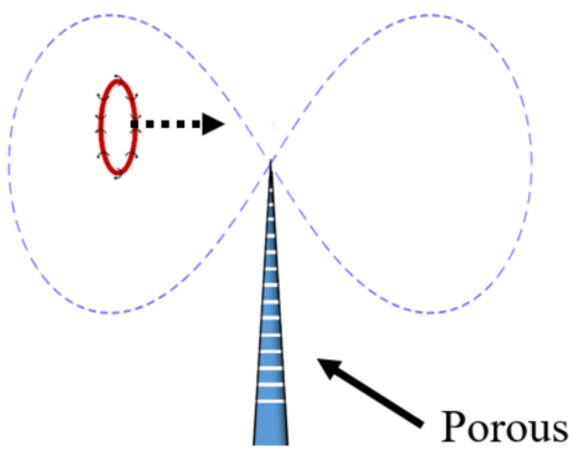

Figure 2.5: Acoustic dipole directivity from a vortex ring convecting near the edge of a non-compact rigid porous plate

Chapter 3

Methods

3.1 Approach

The objective of this chapter is to first a) clarify the variables required to validate the aero-acoustic scaling laws, and then b) introduce an overview of the experiment and how it was designed to capture those measurements. In addition to source waveforms and directivity, Jaworski and Peake [33] and Chen et al. [1] indicate TE sound pressure scaling as $p \sim U^{n/2}L^{m/2}$, where p radiated noise from the turbulent source interacting with the edge. This section will detail how the variables, U,L, and p are a) acquired to empirically test the aforementioned predictions and b) used to compute source waveforms and directivity.

This work, which follows the experimental setup seen in 3.1, generates a turbulent eddy, in the form of a vortex ring (VR), from a vortex ring generator (VRG). The convection speed of the VR was captured with high speed Schlieren. This satisfies measurements to acquire U. To generate the TE noise a plate with a sharp edge is placed in close vicinity to the pseudo-linear pathway of the VR. The interaction of the plate edge and the VR generate the TE noise, p_i. This sound radiation is then captured with a 12 microphone array central to the source region. With these two measurements we are then able to proceed to test the theoretical and computational predictions. Apart from these core measurements, additional instrumentation recorded other characteristics within the system that will be expanded upon in the following sections.

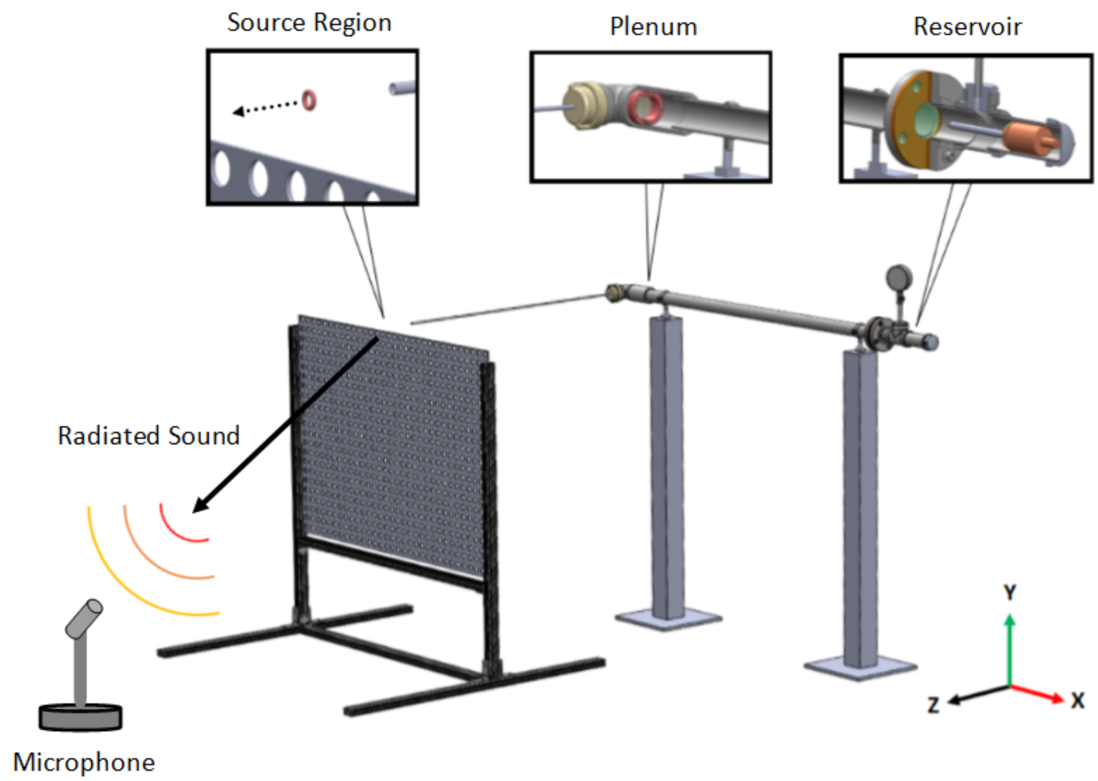

Figure 3.1: A schematic of the experimental setup, details shown for the vortex ring generator plenum, reservoir, source region, and microphones.

3.2 Experimental Setup

3.2.1 Anechoic Chamber

Acoustic measurements were acquired within the Garfield Thomas Water Tunnel's (GTWT) anechoic chamber at the Applied Research Laboratory at The Pennsylvania State University. The chamber dimensions are 5.5m wide, 6.9m deep, and 9.3m high and the room is surrounded by 0.6m x 0.6m x 0.91m fiberglass wedges. The chamber meets IEC 268 and ISO 3745 (ANSI S12.55) standards for frequency ranges from 80Hz to 12.5kHz. Ambient room temperature was recorded with a Fluke 80TK thermocouple module (Everett, WA. USA).

3.2.2 Vortex Ring Generator

A vortex ring generator (VRG), that used a shocktube diaphragm approach, produced the vortex rings for the experiment. The VRG was mounted on sturdy tripods and an aluminum podium, shown in Figure 3.1 so that the mean height was 54" off the chamber floor. Figure 3.3 show the main components of the apparatus.

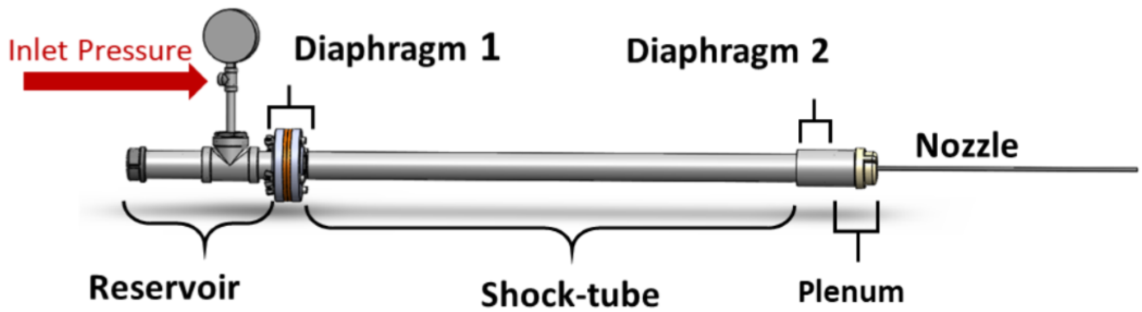

Figure 3.2: A CAD model of the vortex ring generator with the primary components labeled.

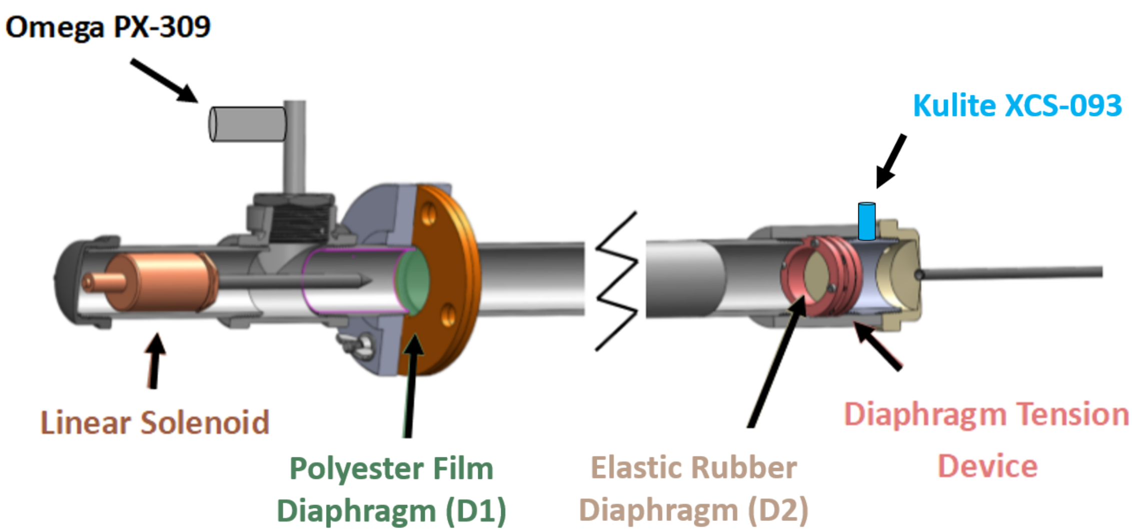

Figure 3.3: A CAD model of the vortex ring generator with the primary components labeled.

The VRG reservoir was supplied with clean compressed air ranging from 358.9kPa to 455.2 kPa to acquire realizations. The reservoir was constructed with a schedule 40 1 1/2" diameter 6" long aluminum pipe, 3x schedule 40 1/4" diameter 3" long copper pipes, 2x aluminum 1/4" to 1 1/2" diameter adapters, and a 4 channel 1/4" iron adapter. The internal volume minus the internal components was $169.6in^3$. The air flow rate was controlled with an inline gas regulator while reservoir pressure was monitored with a mounted Omega PX-309 0-200PSI transducer (Norwalk, CT. USA). This compartment, along with the following components are shown in Figure 3.3.

Clear polyester film (PEF) of thickness 0.002" and 0.0005" (8567K22 and 8567K22, respectively, McMaster Carr, Elmhurst, IL. USA) were used as diaphragm 1 (D1). These were used to separate the reservoir from the shocktube. Housed within the reservoir volume resided a sealed linear push solenoid equipped with a modified GS Outdoors Montec 100-Grain Broadhead (G5, Memphis, MI. USA). Its purpose was to puncture D1 to release a shockwave. Downstream of D1 is a schedule 40 2m long 1 1/2" diameter steel shock tube, with a wall thickness of 0.145" and internal volume of $2279.4cm^3$, that mates to a secondary diaphragm, D2, which undergoes deformation during a test but remains intact after the shockwave interacts with it.

U_R	Reservoir Pressure (kPa)	$D1$	$D2$
39	358.9	PEF 0.0005”	SSR 0.006”
47	375.1	PEF 0.0005”	SSR 0.006”
62	393.3	PEF 0.002”	SSR 0.006”
72	408.7	PEF 0.002”	SSR 0.006”
81	447.5	PEF 0.002”	SSR 0.006”

(a) $\mu/k = 0$

U_R	Reservoir Pressure (kPa)	$D1$	$D2$
45	373.0	PEF 0.0005”	SSR 0.006”
50	381.2	PEF 0.0005”	SSR 0.006”
59	387.6	PEF 0.0005”	SSR 0.006”
66	399.5	PEF 0.002”	SSR 0.006”
74	410.1	PEF 0.002”	SSR 0.006”
79	440.8	PEF 0.002”	SSR 0.006”
86	455.2	PEF 0.002”	SSR 0.006”

(b) $\mu/k = 0.49$

U_R	Reservoir Pressure (kPa)	$D1$	$D2$
41	360.1	PEF 0.0005”	SSR 0.006”
49	379.3	PEF 0.0005”	SSR 0.006”
57	384.6	PEF 0.0005”	SSR 0.006”
62	393.3	PEF 0.002”	SSR 0.006”
66	399.5	PEF 0.002”	SSR 0.006”
73	409.2	PEF 0.002”	SSR 0.006”
79	440.8	PEF 0.002”	SSR 0.006”
83	451.9	PEF 0.002”	SSR 0.006”

(c) $\mu/k = 3.10$

U_R	Reservoir Pressure (kPa)	$D1$	$D2$
45	373.0	PEF 0.0005”	SSR 0.006”
50	381.2	PEF 0.0005”	SSR 0.006”
59	387.6	PEF 0.0005”	SSR 0.006”
66	399.5	PEF 0.002”	SSR 0.006”
74	410.1	PEF 0.002”	SSR 0.006”
79	440.8	PEF 0.002”	SSR 0.006”
86	455.2	PEF 0.002”	SSR 0.006”

(d) $\mu/k = 58.9$

Table 3.1: VRG conditions and diaphragms for measurements. Here, PEF and SSR are abbreviations for polyester film and super-strechable rubber, respectively.

D2 is fitted with 0.006” McMaster super-stretchable rubber diaphragms (SSR), (85995K12, McMaster Carr, Elmhurst, IL. USA) and were placed in tension with a drum-like mechanism produced by the researchers. This diaphragm tension device is shown in Figure 3.4. Downstream of D2 was a 8” long and 1 1/2” diameter acrylic tube that allowed the researchers to observe the behavior of D2 after the shockwave collision, shown in Figure 3.5.

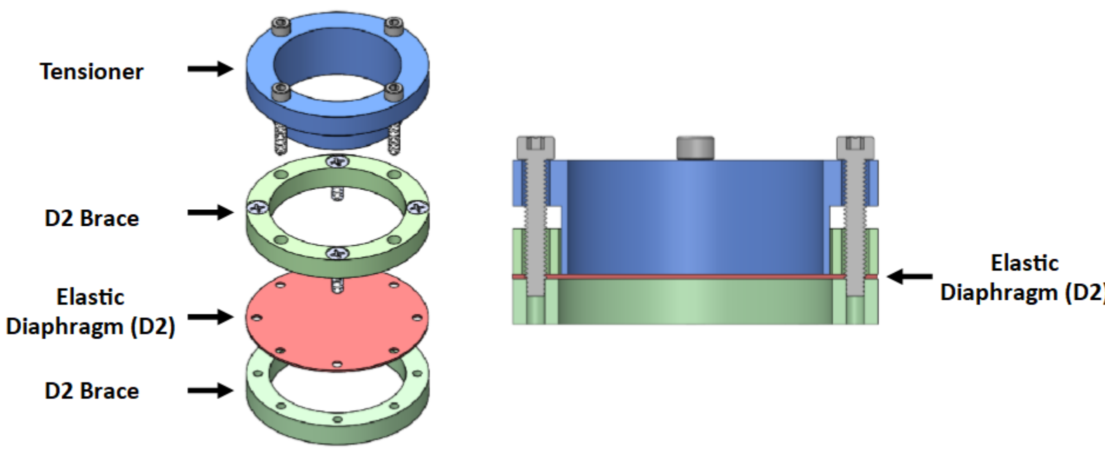

Figure 3.4: An exploded and sectional view CAD drawing of the diaphragm tension device.

A 90 degree rubber coupling after the acrylic tubing then directed the displaced air to the plenum. Plenum pressure was recorded with a Kulite Semiconduction Products Pressure Transducer XCS-093 (Leonia, NJ. USA) mounted flush with the 1 1/2” pipe. Further downstream the 1 1/2” pipe was reduced to a 6mm nipple that connected to an 18” long 6mm in diameter tygon tube that mated to a 40” long 6mm in diameter, H, stainless steel nozzle. The nozzle was isolated from the floor and VRG with rubber material. The nozzle was mounted on a Velmex A40 Series 38” longitudinal traverse (Bloomfield, NY. USA) with 1mm measurement positions which allowed for adjustments in L, the offset distance between the plate edge and nozzle vertically. The VRG conditions required to acquire realizations at every speed are shown in Table 3.1.

3.2.3 Plate Designs

3.2.3.1 Rigid Impermeable Plate

In accordance with the non-compact condition, the aluminum rigid impermeable plate was chosen with dimensions of 48” long, 48” wide, and 0.06” thick. The plate was filed down

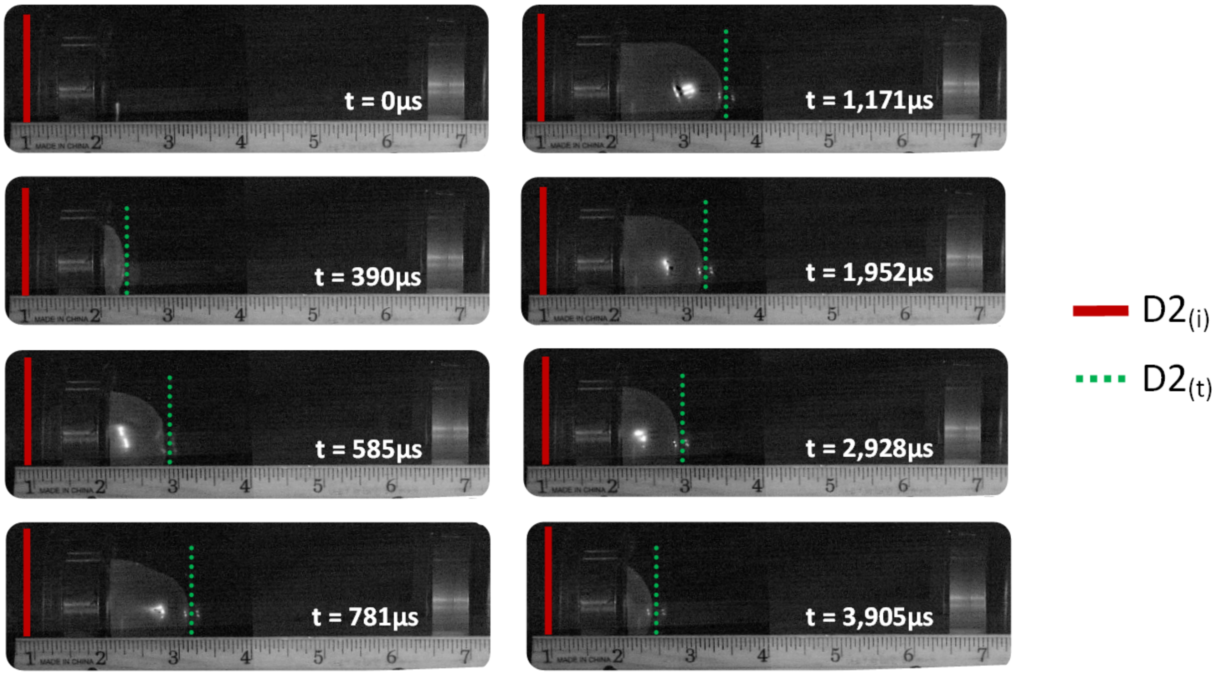

Figure 3.5: Time laps deformation of diaphragm D2 due to collision with shock wave. $D2_i$ is the resting position, and $D2_t$ is the maximum deformation for each time stamp.

uniformly on the edge which interacts with the vortex ring. This edge acted as the TE. The plate was then fitted into an 80/20 frame, seen in Figure 3.1, fixed with 1/4" rubber gasket material to inhibit structural vibrations induced by the vortex ring / plate interaction to transfer to the frame.

3.2.3.2 Porous Plate

In order to span a range of plate porosity between the asymptotic limits identified by Jaworski and Peake[33], listed in Equation 1.1, suitable values of μ/k were chosen for COTS perforated plates by choosing combinations of available plate open area α and hole size R. With dimensions the same as the rigid impermeable plate, characteristics of the porous plates are presented in Table 3.2. Measurements were collected for vortex ring speeds ranging from 39 m/s to 86 m/s. These predictions are presented in Figure 3.6 and Figure 3.7. The mean value of the μ/k range will be used to identify each plate for the rest of this document.

Plate ID	α	Hole Diameter	Edge Thickness	Plate Thickness	Estimated μ/k
1	0	N/A	1.52mm	1.52mm	0
2	0.55	3/4”	1.52mm	1.52mm	0.33 to 0.64
3	0.68	5/32”	1.52mm	1.52mm	2.04 to 4.14
4	0.38	0.0041”	1.52mm	0.066mm	45.4 to 72.3

Table 3.2: Characteristics of plates used in this study.

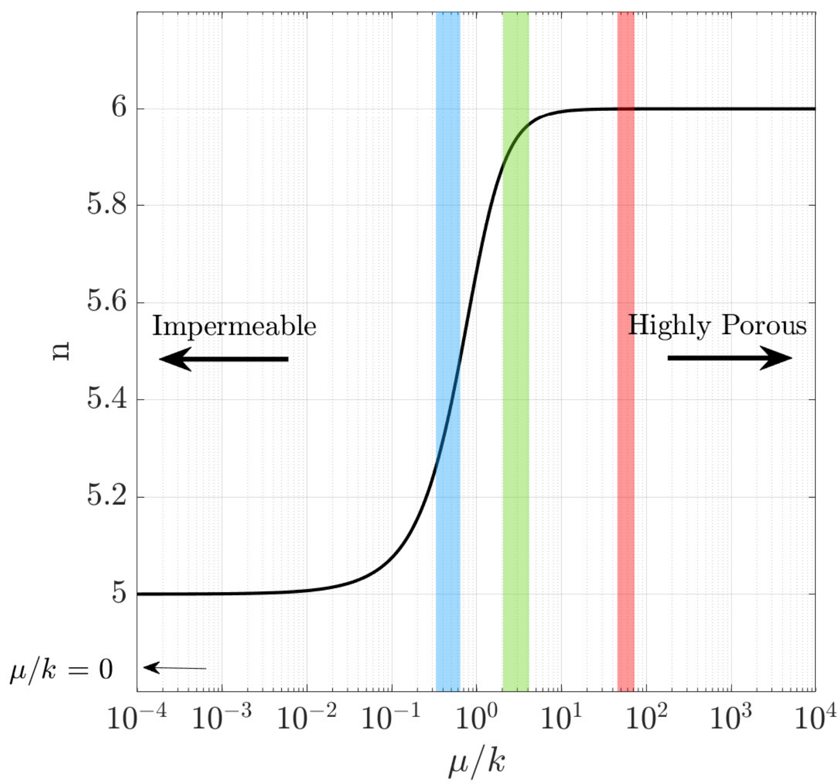

Figure 3.6: Predicted changes in acoustic radiation with plate porosity for power law exponent, n. Colored bands indicate approximate ranges of porosity for the plates listed in Table 3.2.

3.2.4 Schlieren High Speed Imaging

The vortex fluid motion was captured with a Z-configuration Schlieren setup. An overlay of the Schlieren light path is shown in Figure 3.8. The light source, a THOR LABS T-Cube LED Driver (LEDD1B), was positioned 1 focal distance, 0.58m, away from a 6” f/8 parabolic mirror. At this offset distance the light hitting the mirror was reflected into a collimated

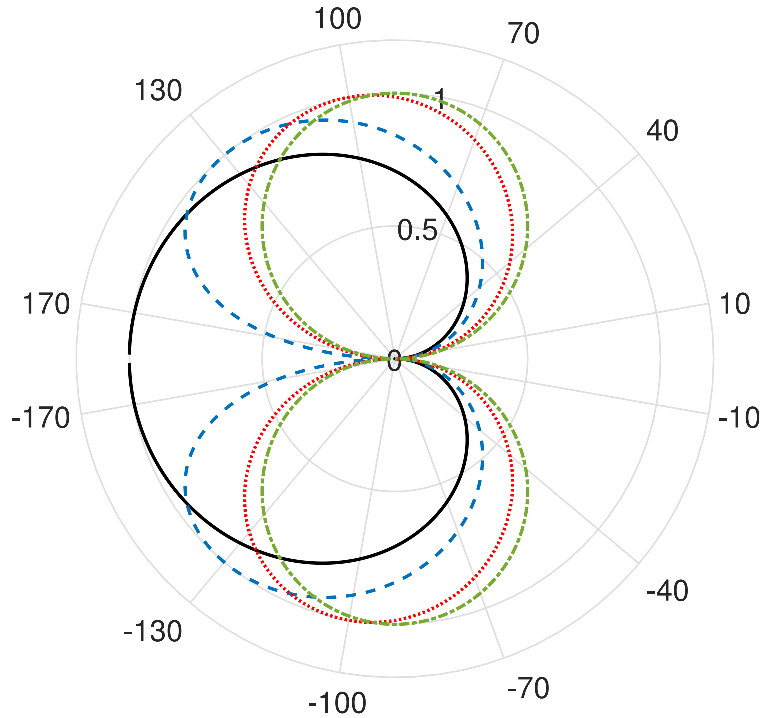

Figure 3.7: Predicted changes in acoustic radiation directivity with plate porosity at each plate listed in Table 3.2. Here, the solid (–) refers to $\mu/k = 0$, (- -) $mu/k = 0.49$, (-.) $\mu/k = 3.10$, and (-:) $\mu/k = 58.9$.

beam that traveled through the test section and onto another identical mirror. When a source is present within the test section with a different refractive index, like the vortex ring, it bends the light off angle from the collimated beam.

The light then travels from the test region onto a second parabolic mirror. This mirror is positioned slightly off angle from the collimated beam and is focused onto a knife edge 1 focal distance away, 0.58m. At this point, light unaltered in the test section can be "cut-away" while impacted light continues past the knife edge. This light then passes through a 200mm Nikon lens, positioned 0.14m away from the knife edge, and onto the photo chip of a Vision Research Phantom v1610 high speed camera. The camera settings are adjusted within Phantom Camera Control Software and set to 1μsec exposure, 896x512 resolution, and a frame rate of 25.6kHz. Calibration was performed with a calipers imaged in the source region to determine the pixel per millimeter ratio.

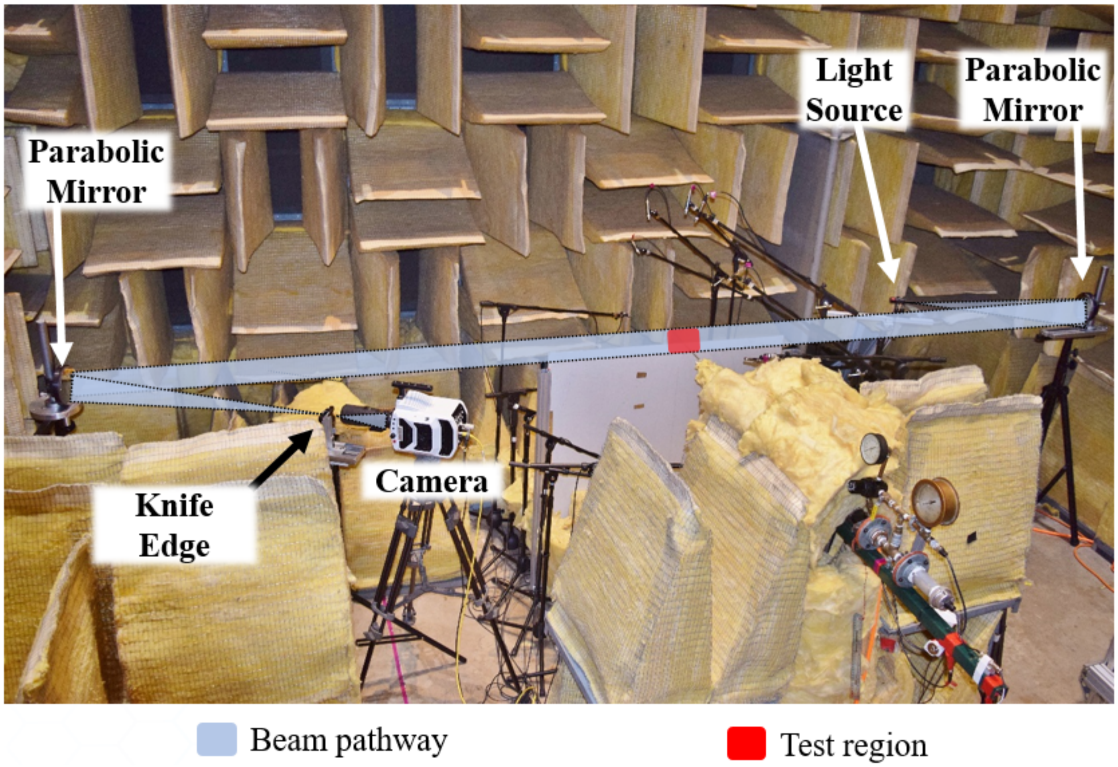

Figure 3.8: Z-configuration Schlieren setup within the anechoic chamber where the blue-gray overlay shows the optical path.

3.2.5 Microphones

The radiated noise from the vortex ring interacting with the plate edge was captured with a 12 microphone circular array. These microphones were 1/2" PCB Piezotronics model 378 B02 models with a frequency range ($\pm 2dB$) from 3.75Hz to 20kHz. Prior to testing, these microphones were calibrated with a Bruel & Kjaer model 4231 sound calibrator. Microphones were carefully positioned radially at 500mm over a series of angles (θ) shown in Figure 3.9. The uncertainty was $\pm 3mm$ and $\pm 5°$ for radial distance and angle, respectively.

3.2.6 Data Acquisition Hardware

Data acquisition (DAQ) hardware and software were a result of products from National Instruments (NI). Signals from the sensors were ported to a NI 9188 chassis with supporting NI 9234, NI 9237, and NI 9239 cards. The microphones and trigger were connected to the NI 9234 cards. The Omega pressure transducer was attached to the NI 9237. Lastly, the Kulite

Figure 3.9: The 12 microphone array positioned central to the source region in the anechoic chamber.

pressure transducer was attached to the NI 9239 card. The software used to process these signals was LabVIEW NXG 5.0 2020 (Austin, TX. USA). A sample frequency of 51.2kHz was utilized across DAQ channels, which allowed for the VR frequency to be resolved. The synchronization and simultaneous Schlieren high speed imaging was performed by an output TTL pulse from the NI chassis. This signal was sent to a Berkley Nucleonics Pulse Delay Generator Model 555 with a $f_s/2$ frequency divider, where f_s is the DAQ sample rate, changing the output frequency to 25.6kHz. This excitation channel connected to a frequency sync on the Vision v1610 camera. For the v1610 camera, frame rates above 30kHz are possible only if imaging is performed on a fraction of the chip, so there is a trade off between field of view size, spatial resolution, and frame rate. In order to maximize field of view and image spatial resolution, the camera used a frame rate half that of the pressure sampling.

3.2.7 Test Procedure

The test procedure for the experiment for a single case proceeded as follows. First the DAQ and high speed camera systems are armed. The VRG reservoir pressure regulator is opened and pressure is monitored with the Omega 309 pressure transducer. When driving pressure conditions are met, see Tables 3.1a through 3.1d, the inlet regulator is closed and pressure remains constant. A 5V TTL pulse from an external trigger then initiates the data collection process. After 0.25sec delay the linear solenoid actuates and the puncture rod is accelerated to rupture D1. The rupture of D1 causes the shock wave to propagates down the shocktube and collide with D2. The collision causes D2 to deform, as illustrated in Figure 3.5, but remain intact. Deformation of D2 compresses the air in the plenum, giving rise to a sharp pressure peak, measured by the Kulite XCS 093 transducer. This compression ejects a slug of air from the nozzle. First a spherical shockwave followed by a jet-like pulse that forms into the vortex ring. The vortex ring approximately 6.5mm in radius, then convects in a linear path over the edge producing a pulse of sound. This entire process is captured with the Schlieren high speed camera. This process is repeated for each vortex ring speed. Five realizations are acquired for each speed, and then ensemble-averaged.

3.3 Data Acquisition and Signal Processing

Measurements were collected and processed with scripts, see Appendix A written in Matlab 2021 (Mathworks, Natick, MA. USA). Figure 3.10 shows the time series of events that occurring during a single realization. Here, the top subfigure shows the puncture of D1 at approximately 0.321sec. Immediately a decrease in reservoir pressure occurs. After a short delay, due to the propagation time of the shockwave in the shocktube, the deformation of D2 causes a spike in plenum pressure, observed in the middle plot at approximately 0.327sec. As pressure in the plenum builds a spherical shockwave is emitted from the nozzle and shortly after a vortex ring. These signatures are observed in the *bottom* plot at approximately 0.332sec and 0.333sec, respectively.

3.3.1 Radiated Noise Measurements

In Kambe et al.[11], the authors remove excessive background noise, associated with the mechanical noise of their vortex ring generator and the inherent shockwave contributions with a subtraction method. This approach acquired sound pressure measurements at all 12 microphones for two cases: (1) vortex ring convecting over the plate edge at a given speed, and (2) the vortex ring blocked, inhibiting ring formation and removing the ring/edge interaction sound, so that the acoustic singals contain only VRG mechanism noise and

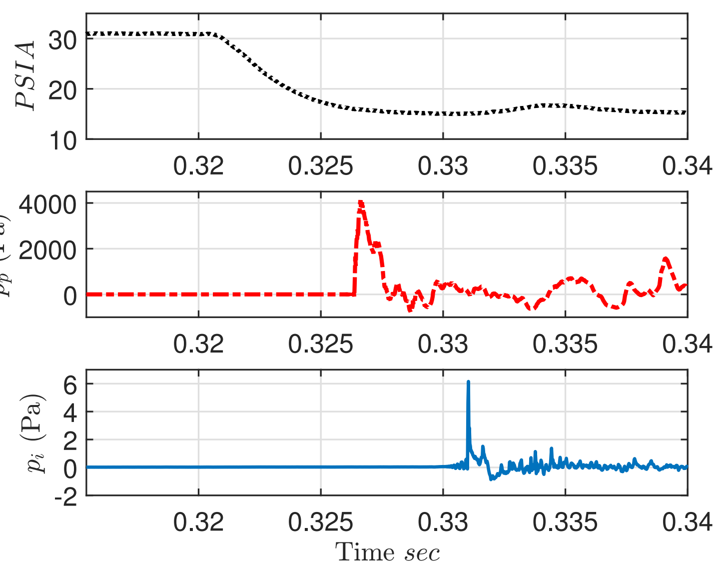

Figure 3.10: Overview of time series of events observed by the reservoir pressure gage (top), plenum pressure transducer(middle), and a radial microphone ($\theta = -170, r = 500mm$) (bottom)

effects of the shock waves. The subtraction of B from A would yield a waveform solely comprised of contributions from the vortex ring interacting with the plate (i.e the undesirable contributions from shockwaves and mechanism noise were subtracted off).

This experiment ran a similar series of tests to Kambe et al.[11] which are presented in Figure 3.11. The figure will first be discussed in regards to the ensembled-averaged vortex ring condition. The spherical shockwave emitted from the nozzle prior to the vortex ring formation is the first prominent signal received by the microphone, shown as S_1 at approximately 750 μsec. As the spherical shock propagates away from its source, at the nozzle, it is reflected by the large plate and then back to the microphones. This additional propagation distance delays the reflected shockwave from the plate, shown as S_2 at approximately 980 μsec from S_1. During this period of time the fully developed vortex ring begins to interact with the edge of the plate, and the radiated noise is observed as VR at approximately 1100 - 1700 μsec. Residual reflections from shock waves S_1 and S_2 continue to reflect in the test section, which are observed as large spikes indicated as S_3 at approximately 2400 μsec seen in the vortex ring realization case. For the obstruction conditional, all of the aforementioned points are seen aside from the vortex ring signal (VR), which is expected. From $\sim 1100 - 1700 \mu sec$ the obstruction condition remains void of apparatus or shock noise

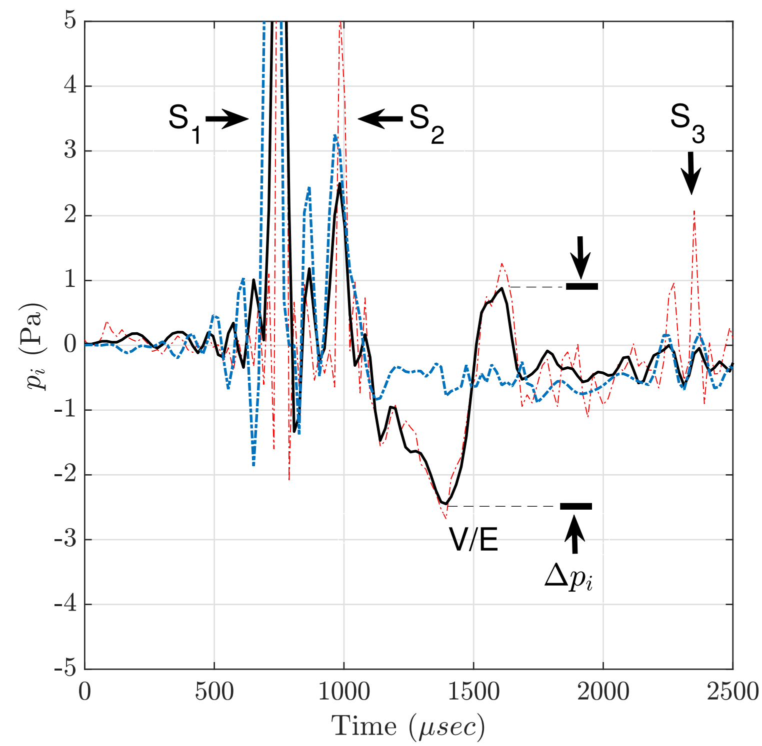

Figure 3.11: Farfield pressure waveform for $\mu/k = 0$, at $U_R = 62m/s$ and $\theta = 70$. The solid line (–) represents the ensembled-averaged signal, (- -) the ensembled-averaged obstruction signal, and (-.) a single realization of acoustic pressure when a vortex ring also convects over the edge. V/E is the vortex plate edge interaction, S_1 the spherical shock wave emitted from the nozzle prior to vortex ring formation, S_2 the rebound of the spherical shock off the plate, VR the vortex ring signal, S_3 residual shock reflections in the test setup, and Δp_i the peak-to-peak of the ensembled-averaged VR signal.

confirming the method proposed by Kambe et al.[11] is possible. However, since the measurements of the obstruction case and vortex ring ensemble-average, remains relatively quiet from S_2 to S_3, the authors capitalized on this *quiet-zone* to acquire the vortex ring realizations. Since the vortex signal is dependent upon the vortex ring speed adjustments to Z_p were made if necessary. These conditions, along with the estimated μ/k, U_R, and L, are presented in Table 3.3. Lastly, the Δp_i associated to the vortex ring, as shown in Figure 3.11 was recorded as the the peak-to-peak value of VR.

3.3.2 Estimation of vortex ring speed

The speed of the vortex ring, i.e. U_R, was determined from the use of high speed Schlieren. Since the high speed imaging system and DAQ systems were synchronized, the pre-formation, formation, and convection path of the vortex ring near the edge were recorded, as shown in Figure 3.12. The position of the vortex ring was determined manually in post-process, see Appendix A, by recording the pixels at the top and bottom of the core. Both points were then averaged to provide the mean x position (pixel) of the vortex ring. This process was performed on 25 incremented frames for each realization. To convert the pixels to mm, the experiment utilized a cal-image which had a known distance, via a pair of calipers in the source region, to acquire the Δpixel per mm. This conversion was then applied to the Δpixels to determine the vortex ring position. The result from a realization is shown in Figure 3.13. To determine the speed of the vortex ring, a linear fit was applied to the data points from $x = 2mm$ to $x = (Z_p - n_d)$. The lower limit $x = 2mm$ ensured the vortex ring was fully developed. The terminal point, where $x = (Z_p - n_d)$, was used to account for the potential loss in speed of the vortex ring as it interacts with the plate.

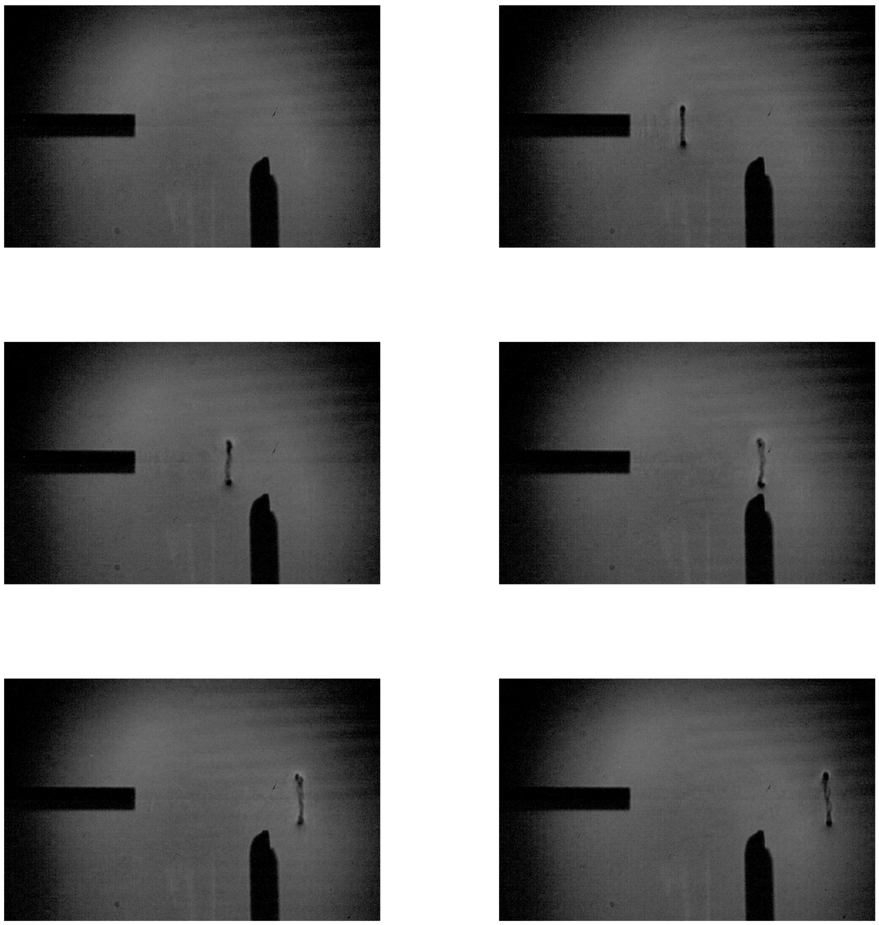

Figure 3.12: Schlieren high speed imaging of vortex ring formation and convection pathway near the plate when U_R = 62 m/s, L = 9.8mm, and Z_p = 54mm.

U_R	$L(mm)$	$Z_p(mm)$	Estimated μ/k
39	9.8	47	0
47	9.8	47	0
62	9.8	54	0
72	9.8	54	0
81	9.8	54	0

(a) $\mu/k = 0$

U_R	$L(mm)$	$Z_p(mm)$	Estimated μ/k
45	9.8	47	0.64
50	9.8	47	0.57
59	9.8	47	0.48
66	9.8	54	0.43
74	9.8	54	0.39
79	9.8	54	0.36
86	9.8	54	0.33

(b) $\mu/k = 0.49$

U_R	$L(mm)$	$Z_p(mm)$	Estimated μ/k
41	9.8	56	4.14
49	9.8	56	3.47
57	9.8	56	2.98
62	9.8	56	2.74
66	9.8	56	2.57
73	9.8	56	2.33
79	9.8	56	2.15
83	9.8	56	2.04

(c) $\mu/k = 3.10$

U_R	$L(mm)$	$Z_p(mm)$	Estimated μ/k
54	9.8	54	72.3
60	9.8	54	65.1
65	9.8	54	60.1
72	9.8	54	54.2
78	9.8	54	50.1
82	9.8	54	47.6
86	9.8	54	45.4

(d) $\mu/k = 58.9$

Table 3.3: Case conditions for measurements at a) $\mu/k = 0$, b) $\mu/k = 0.49$, c) $\mu/k = 3.10$, and d) $\mu/k = 58.9$.

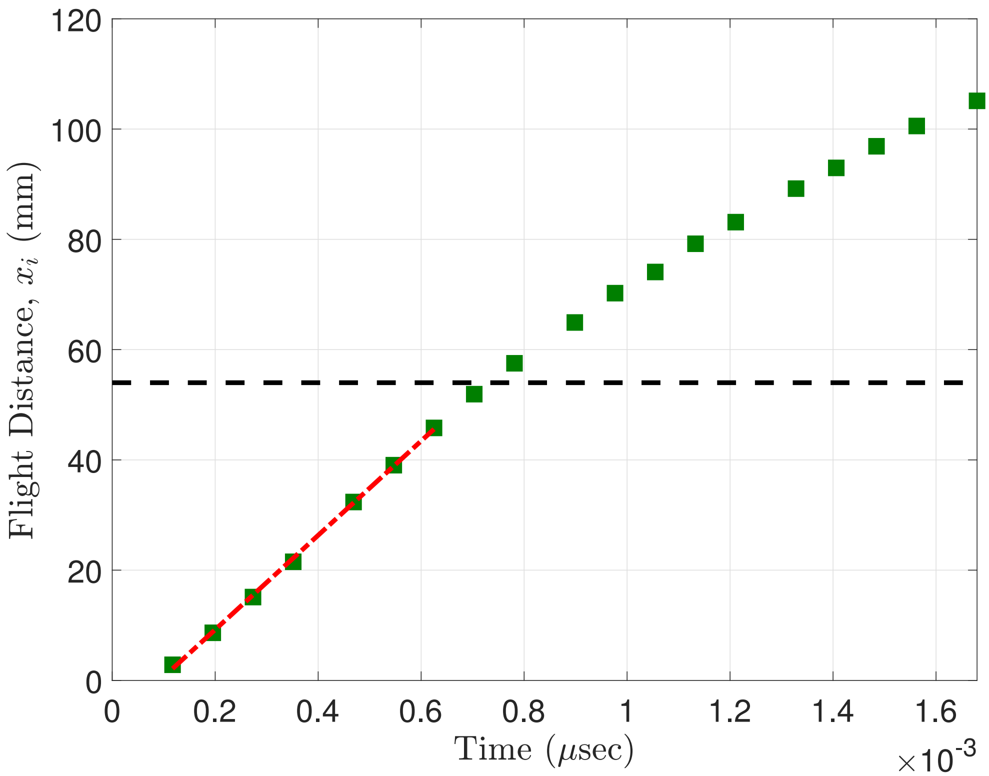

Figure 3.13: Vortex ring speed (U_R) determined from the high speed Schlieren image analysis. □ indicate the mean vortex ring location (x_i) at time step (t), (- -) the linear fit to determine (U_R), and the horizontal dashed line (- -) is the edge location. For this realization U_R is 83 m/s, $Z_p = 56$ mm and $\mu/k = 3.10$.

Chapter 4

Results

This chapter provides a summary of the measurements collected in the vortex ring/plate study. First an overview of the vortex ring motion will be addressed along with the measurement conditions for each ensemble. Following will be the farfield pressure waveforms, radiated sound power scaling ($U^{\bar{n}}$), normalized directivity, sources waveforms, and lastly impact distance scaling (L^m). Furthermore, these aforementioned sections will present the data for the baseline case, and then progress to the porous plates.

4.1 Vortex Ring Motion

A summary of the vortex ring motion analysis is presented in Figure 4.1 for plate 2, or μ/k = 0.49. Here the results show as the vortex ring speed increases the convection time of the vortex ring to reach $x = (Z_p - H)$ is reduced. This results is readily evident by the slopes from the linear fits. This expected result was observed for all plates tested.

4.2 Farfield Pressure Waveforms

The farfield pressure waveforms will now be presented and discussed in the following subsections. The waveforms for each plate are shown in Figure 4.2 where the left and right columns represent $-\theta$ and $+\theta$ microphone positions, respectively. Additionally, it can be noted the (VR) signal is constrained to the *quiet-zone*, as mentioned in the previous section.

Theoretical predictions and experimental findings, mentioned in Chapter 1, indicate a $sin(\theta/2)$ directivity, i.e. cardioid, for a turbulent source interacting with a rigid impermeable

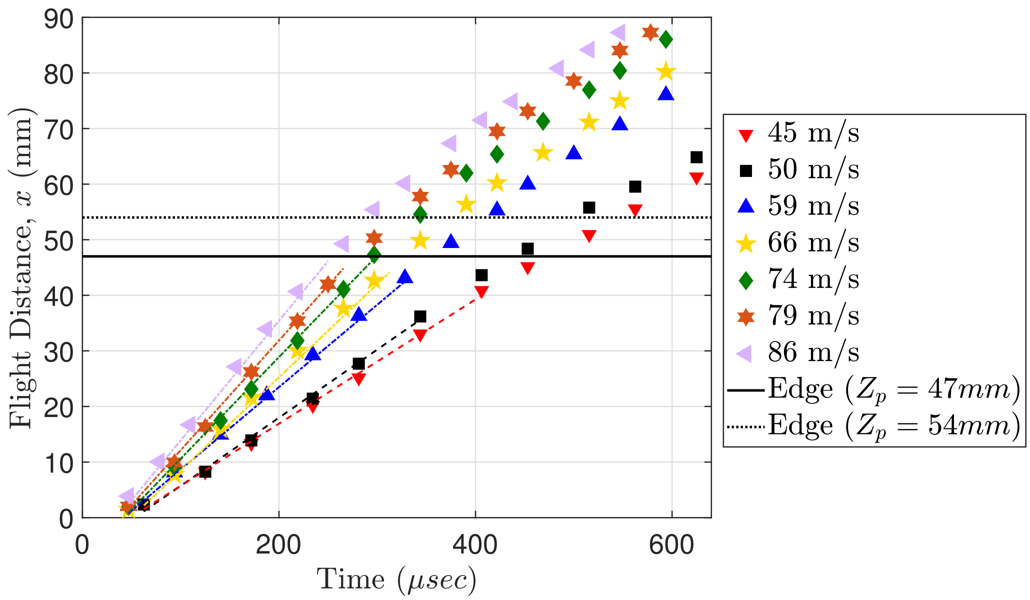

Figure 4.1: Vortex ring motion for different ring speeds for $\mu/k = 0.49$ at fixed $L = 9.8$mm. Vortex ring position (x) vs time. Data points obtained from high-speed video analysis. Dot-dashed lines (-.) indicate linear fits up to dotted line (:) $Z_p = 54$mm. Dashed lines ($--$) indicate linear fits up to solid line ($-$) $Z_p = 47$mm. The slope of the dot-dashed (-.) and dashed ($--$) lines provides an estimate of ring approach speed, U_R.

plate. This considered the expected pressure maxima would occur at $\pm 180°$, with a monotonic decay as θ approaches 0. The results in Figure 4.2 a) show this type of trend where the pressure maxima occur at high $\pm 170°$ and decrease as θ approaches 0. Additionally, the positive to negative sinusoidal waveforms and negative to positive sinusoidal waveforms for column left and right, respectively, suggests the $sin(\theta/2)$ relationship.

As μ/k increases from 0 to 0.49 Jaworski and Peake[33] and Chen et al.[1] predict a) reductions in radiated sound and a near cardioid / weak dipole acoustic directivity. These transitions are associated to an increase in the nearfield acoustic transparency. In Figure 4.2 b), where $\mu/k = 0.49$, the most obvious observation is the change in waveforms compared to Figure 4.2 a). Here it is shown the measured noise at $\pm 170°$ is reduced, suggesting the formation of a second null - a characteristic of the dipole. Furthermore, the measured Δp_i for nearly all θs is reduced, compared to Figure 4.2 a), even though the U increased from 81 m/s to 86 m/s. These results show an increased μ/k reduces the radiated noise at nearly equivalent speeds, and there are observable differences in sound directivity.

As μ/k, now at ~ 3.10, continues to increase the effect of the nearfield acoustic trans-

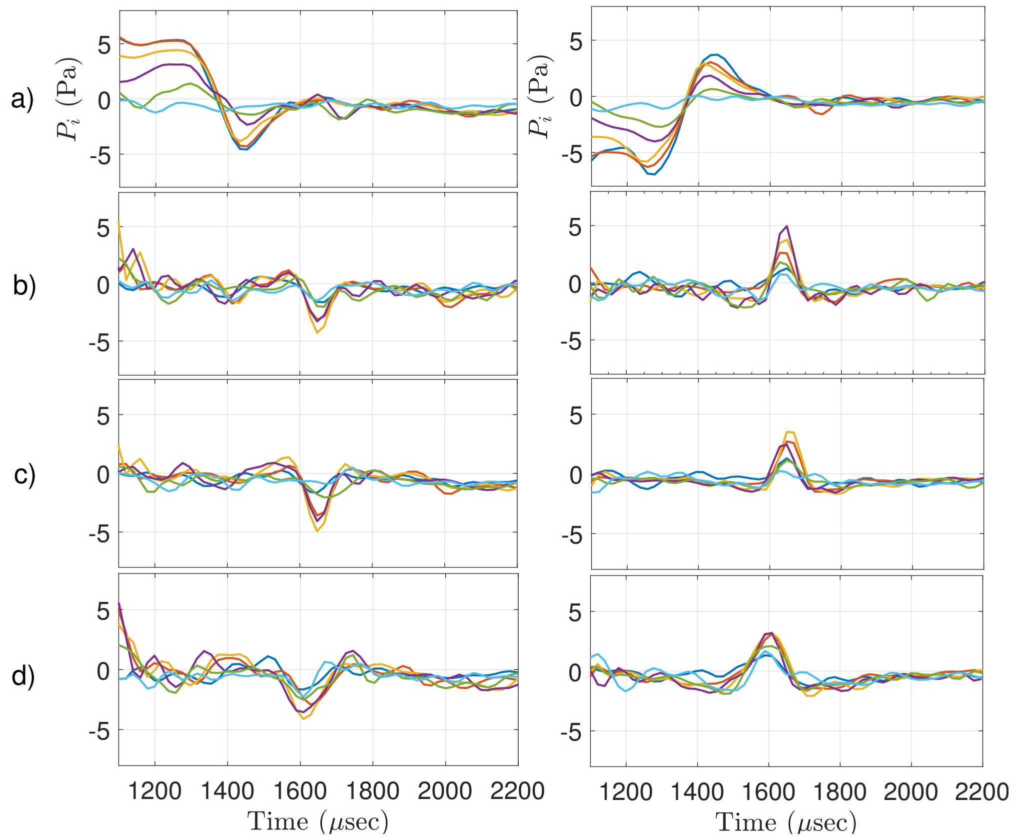

Figure 4.2: Sound pressure waveforms $p_i(\theta)$ for (a) $\mu/k = 0$, 81 m/s, (b) $\mu/k = 0.49$, 86 m/s, (c) $\mu/k = 3.10$, 79 m/s, and (d) $\mu/k = 58.9$, 86 m/s. Right column: $\theta > 0$, left column $\theta < 0$, – $\pm$ 170°, – $\pm$ 130°, – $\pm$ 100°, – $\pm$ 70°, – $\pm$ 40°, – $\pm$ 10°.

parency becomes more significant. Jaworksi and Peake[33] and Chen et al.[1], predict for a $\mu/k = 3.10$ a weak cardioid / near dipole behavior should be observed. In Figure 4.2 c), where $\mu/k = 3.10$, it is again observed the sinusoidal waveform, present in case a), to be removed. Additionally, as in case b) the measured noise at ±170° is reduced, again suggesting the formation of the second null of the dipole. Lastly, it is observed the measured noise in case c) is reduced compared to case a).

The last plate tested had a μ/k of 58.9, where results are shown in Figure 4.2 d). At this condition Jaworksi and Peake[33] and Chen et al.[1], predict a dipole directivity. As with cases b) and c) it is observed the radiated noise measured at ±170° is reduced. This indicates the second null of the dipole to take form.

4.3 Radiated Sound Power Scaling

This section presents empirical estimates of the sound power scaling with velocity, and compares theoretical predictions to them. Recalling that sound power $\Pi_{rp} \sim \Delta p_i^2 \sim U_R^n$, Figure 4.3 a log-log plot of Δp_i^2 vs ring speed U_R. A power-fit, in the form $b * U_R^n$, is applied to each θ to determine the sound power exponent $n(\theta)$. These values along with their respective R^2 are reported in Table 4.1. Results from $\theta = \pm$ 10 were omitted due to their low signal to noise ratios, as they were positioned in the null of the cardioid and dipole. For $\mu/k = 58.9$ results from $\theta = \pm$ 170 were not included because the signal-to-noise ratio was low in the directivity null.

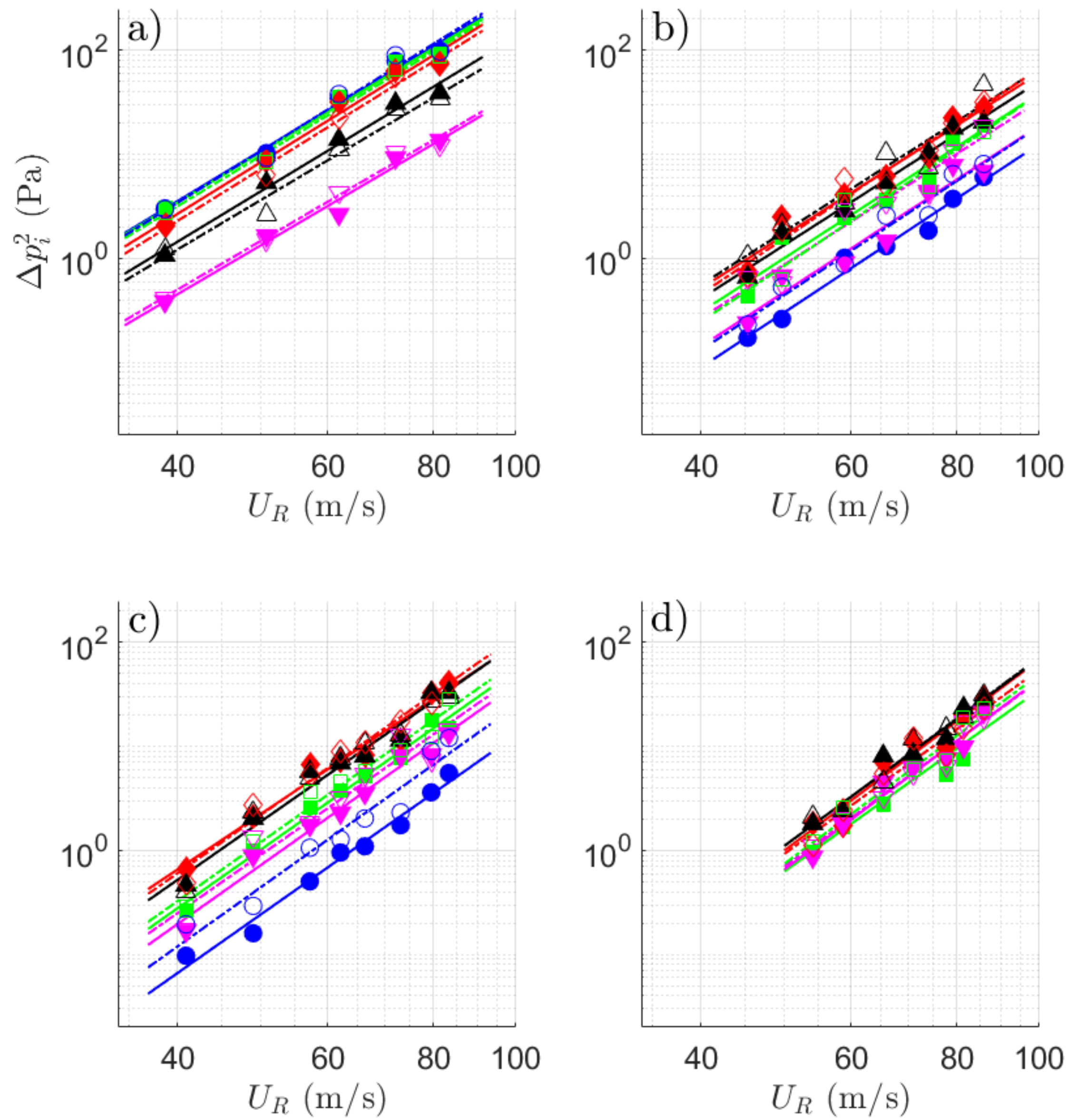

Figure 4.3: Sound power ($\sim \Delta p_i^2$) versus vortex ring speed (U_R) to estimate power law exponent $\bar{n}$. Plot (a) $\mu/k = 0$, (b) $\mu/k = 0.49$, (c) $\mu/k = 3.10$, and (d) $\mu/k = 58.9$. The unfilled and filled symbols represent ◯ ±170, □ ±130,◇ ±100,△ ±70,▽ ±170, respectively. Low signal to noise conditions have been removed. Power-fit curves are shown for all microphones with the aforementioned color code and with solid (-) and dashed (- -) lines for positive and negative θ, respectively.

4.3.1 Sound Radiation Power Law Exponent

The radiated sound power for a rigid impermeable plate has been shown theoretically [2;33] and experimentally [12;11;13;14;15;16] to scale as $\Pi_{rp} \sim U^5$. The baseline case for this experiment examines the scaling behavior for this plate type and is shown in Figure 4.3 a). Here, it is observed at $\pm 170°$, i.e the solid and open blue circle markers, produce – in most cases – the maximum pressure at each ensembled-averaged speed. This indicates the rigid impermeable edge effectively acting as a baffle as previous works suggested. Table 4.1 a) shows the power law exponent n_i for each angular microphone position θ_i, with a mean value of $\bar{n} = \mathbf{4.98}$. These results are in strong agreement with Ffowcs-Williams and Hall [2] U^5 and Kambe et al. [11] $U^{5.06}$.

As the porosity increases, theoretical predictions by Jaworski and Peake [33] and Chen et al. [1] show sound power scaling to transition from U^5 to U^6 for rigid impermeable to rigid highly porous, respectively. This transition was shown in Figure 3.2 with the overlaid ranges for the plates tested. The results for this experiment will now be discussed.

The first plate reported in this section is the low μ/k plate, plate 2 where the predicted sound intensity scaling ranges $U^{5.25-5.59}$. Figure 4.3 b) and Table 4.1 a) show the results for the experiment. In Figure 4.3 b) it is observed the $\pm 170°$, i.e the solid and open blue circle markers, measure much less in amplitude compared to the other microphones. This indicates, as noted in Chapter 4.2, that a null formation occurred at $\pm 180°$. Additionally, the Δp_i^2 for the microphones is much less than the rigid impermeable condition. This shows, in general, that at an identical speed the noise produced by the vortex / plate for the porous case is much quiet than the impermeable. This is confirmed in Table 4.1 a), which shows the sound power scaling for every microphone (n_i), where the mean sound power $\bar{n} = \mathbf{5.32}$.

Next the $\mu/k = 3.10$ plate, will be discussed where the predictions for the sound intensity scaling range from $U^{5.87-5.96}$. Experimental results for this condition are shown in Figure 4.3 c) and Table 4.1 b). In Figure 4.3 c) once again we observe the $\pm 170°$ microphones measure very little noise compared to the other microphones. This again shows the null at 180°. Less evident from Figure 4.3 is whether the sound intensity scaling has decreased between plates $\mu/k = 0.49$ and $\mu/k = 3.10$. Table 4.1 b) shows the sound power scaling as $\bar{n} = \mathbf{5.72}$. This shows the radiated noise decreases inversely proportional to μ/k.

Lastly the high μ/k plate, plate 4 is presented where the predictions for the sound intensity scaling are U^6. The experimental results for this condition are shown on Figure 4.3 d) and Table 4.1 c). As before, Figure 4.3 d) shows the measured Δp_i for $\theta = \pm 170$ to be

θ	n_i	R^2
-170	4.94	0.9981
-130	4.92	0.9965
-100	5.06	0.9953
-70	4.94	0.9942
-40	4.80	0.9752
40	4.77	0.9845
70	4.84	0.9853
100	5.09	0.9971
130	4.94	0.9962
170	5.07	0.9958

(a) $mu/k = 0$

θ	n_i	R^2
-170	5.39	0.9612
-130	5.27	0.9707
-100	5.20	0.9723
-70	5.25	0.9847
-40	5.33	0.9187
40	5.24	0.9634
70	5.21	0.9731
100	5.44	0.9893
130	5.49	0.9713
170	5.40	0.9597

(b) $mu/k = 0.49$

θ	n_i	R^2
-170	5.74	0.9520
-130	5.74	0.9828
-100	5.60	0.9834
-70	5.70	0.9816
-40	5.77	0.9626
40	5.70	0.9588
70	5.72	0.9783
100	5.71	0.9866
130	5.77	0.9740
170	5.80	0.9360

(c) $mu/k = 3.10$

θ	n_i	R^2
-130	5.82	0.9737
-100	6.12	0.9625
-70	6.00	0.9670
-40	6.09	0.9731
40	5.96	0.9876
70	6.04	0.9477
100	5.9	0.9644
130	6.06	0.9799

(d) $mu/k = 58.9$

Table 4.1: Sound power exponent, n_i, for each microphone at (θ_i) for a) $\mu/k = 0$, b) $\mu/k = 0.49$, c) $\mu/k = 3.10$, and d) $\mu/k = 58.9$.

very small in magnitude compared to the other θ, and therefore in the dipole null created by the acoustically transparent plate. As explained prior, in regards to $\pm 10°$, the signal to noise ratio in the nulls becomes very small, and therefore the confidence in the $\theta = \pm 170$ diminishes. Thus these values were omitted when calculating $\bar{n}$ for this condition and yield a sound power scaling as $\bar{n} = \mathbf{5.99}$.

4.3.2 Radiated Sound Power Exponent - Comparison of Theory to Experiment

The objective of this section is to determine the agreement between the experimental measurements and theoretical predictions of Jaworski and Peake[33] and Chen et al.[1]. These findings are shown in Figure 4.4. Here it is observed the trend of the theoretical predictions aligns with the experimental findings. It is shown the radiated sound intensity from the vortex ring / plate interaction from rigid porous plates is significantly less than that of a rigid impermeable plate at identical conditions. Furthermore, the theoretical predictions at each μ/k under-predicts the experimentally measured sound intensities. For the rigid impermeable plate, where $\mu/k = 0$, sound power scales as $U^{4.98}$ compared to the theoretical prediction U^5. For $\mu/k = 0.49$, sound power scaled as $U^{5.32}$ compared to the predicted $U^{5.39}$. It must be noted that the predicted $\bar{n}$ is a mean of the upper and lower limits specific to each porous plate. Since the vortex ring speed factors into the value of k, shown in Equation 1.1, the theoretical range of sound power scaling is $U^{5.25-5.59}$. With this assumption, plate $\mu/k = 0.49$ falls within the theoretically predicted range. The sound intensity of $\mu/k = 3.10$ scales as $U^{5.72}$ which is below the μ/k specific theoretical prediction of $U^{5.94}$ and theoretical range $U^{5.87-5.97}$. For $\mu/k = 58.9$ the sound power scaling is predicted to scale as U^6. This is when the effect of near-field acoustic transparency is significant. The experimental sound power scaling at μ/k was $U^{5.99}$, which is in close agreement with the predicted U^6 scaling.

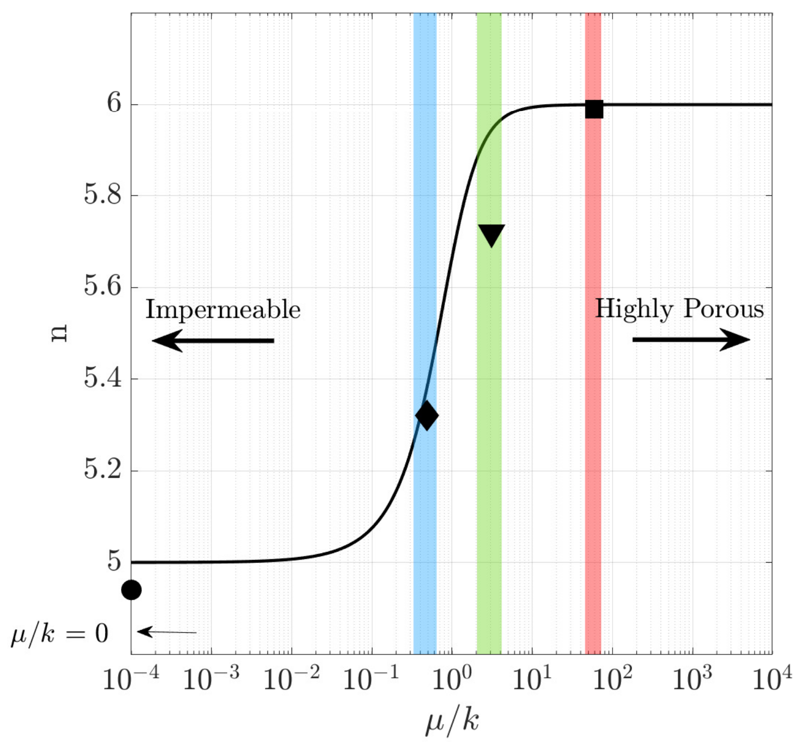

Figure 4.4: Comparison of predicted values of sound power law exponent $\bar{n}$ to measurement. The shaded regions blue, green, and red represent the μ/k ranges for $\mu/k = 0.49$, $\mu/k = 3.10$, and $\mu/k = 58.9$, respectively. The symbols indicate a) $\bigcirc$ $\mu/k = 0$ and $\bar{n} = 4.94$, b) $\diamond$ $\mu/k = 0.49$ and $\bar{n} = 5.32$, c) $\bigtriangledown$ $\mu/k = 3.10$ and $\bar{n} = 5.70$, and d) $\square$ $\mu/k = 58.9$ and $\bar{n} = 5.99$.

4.4 Acoustic Directivity

An overview of the directivity $\beta(\theta)$ of the vortex ring / plate source interaction for the plates tested will now be discussed. These results are shown in Figure 4.5. The radial distance in the polar plots represent $(\Delta p_i/U^{\bar{n}/2})$ normalized by the maximum at each ensembled-averaged condition. For Figure 4.5 a) and d), the directivity is known as $sin(\theta/2)$ and $sin(\theta)$, respectively. The $\beta(\theta)$ for intermediate cases in b) and c), were predicted numerically by collaborators Dr. Justin Jaworski and Huansheng Chen at $\mu/k = 0.46$ and 3.55 for experimental mean values of $\mu/k = 0.49$ and 3.10, respectively.

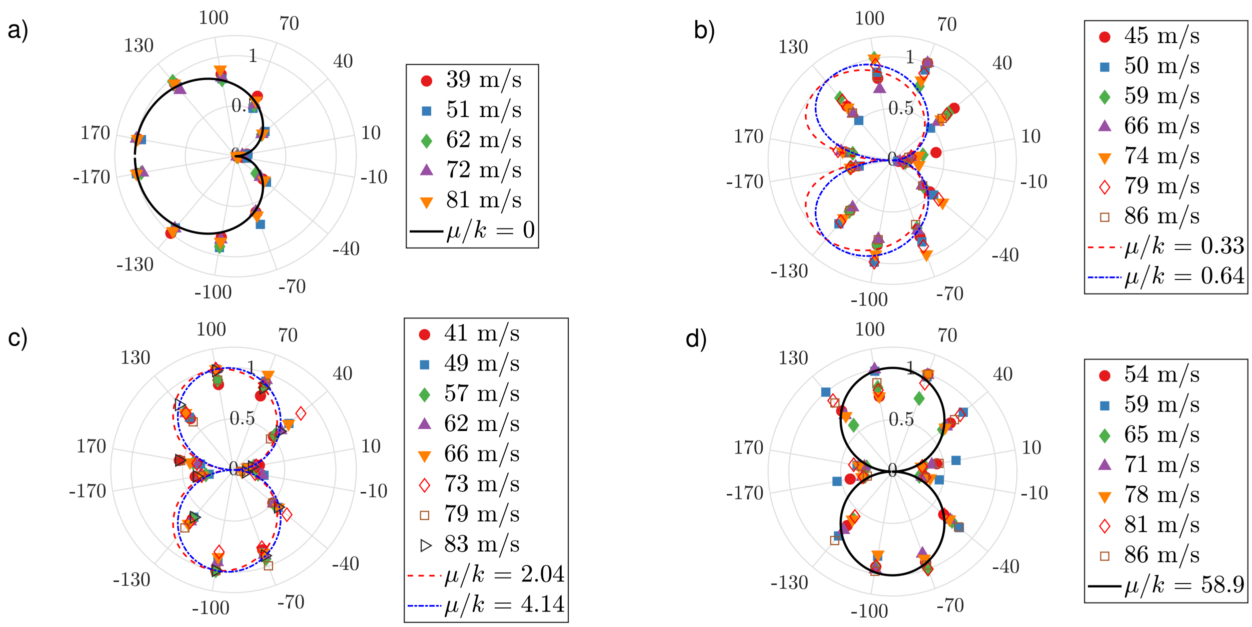

Figure 4.5: Normalized directivity $(\Delta p_i/U^{\bar{n}/2})$ versus θ. For (a) $\mu/k = 0$, where ◯, □, ◇, △, ▽ are 39 m/s, 51 m/s, 62 m/s, 72 m/s, and 81 m/s, respectively. For b) $\mu/k = 0.49$, where ◯, □, ◇, △, ▽, unfilled ◇, and unfilled □ are 45 m/s, 50 m/s, 59 m/s, 66 m/s, 74 m/s, 79 m/s, and 86 m/s respectively. For c) $\mu/k = 3.10$, where ◯, □, ◇, △, ▽, unfilled ◇, and unfilled □, and unfilled ▷ are 41 m/s, 49 m/s, 57 m/s, 62 m/s, 66 m/s, 73 m/s, 79 m/s, and 83 m/s respectively. For d) $\mu/k = 58.9$, where ◯, □, ◇, △, ▽, unfilled ◇, and unfilled □ are 54 m/s, 59 m/s, 65 m/s, 71 m/s, 78 m/s, 81 m/s, and 86 m/s respectively. The solid lines represent the theoretical directivity for each case.

Directivity measurements for the rigid impermeable plate are shown in Figure 4.5 a). The baseline case is consistent with previous findings[2;11], and predictions for porous plates[33;34;1] agree well with our measurements. The cardioid directivity, as $sin(\theta/2)$, shows that the impermeable plate effectively baffles the directivity of the source interaction at ±170°.

As porosity increases from the baseline rigid impermeable plate, the formation of the null at 180° should immediately develop[33;1]. In the low μ/k condition, where $\mu/k = 0.49$, shown in Figure 4.5 b), the theory predicts a skewed dipole directivity, where the skew decreases with increased porosity. Our measurements seem to indicate that while the skewing is observable, it is much less pronounced than predicted. It is shown the theoretical predictions a) under-estimate the experimental radiated noise, from $-70°$ to $+70°$, and b) over-estimate the experimental radiate noise at $-130°$ and $+130°$. Agreement between theory and experiment is observed at $\pm170°$ where the null formation of the dipole develops.

Results from $mu/k = 3.10$, i.e. plate 3, are shown in Figure 4.5 c). As a higher porosity case than b), theoretical predictions[33;1] show less skewing of the dipole. The experimental findings show a more defined null, compared to b), at $\pm170°$, and a slight skew of the dipole pattern. However, the theory under-predicts the radiated noise at $\pm130°$ whereas agreement between the theoretical predictions and experimental findings are observed in other values of θ.

The results from $\mu/k = 58.9$ are shown in Figure 4.5 d). For this highly porous case the theory[33;1] predicts a non-skewed dipole, characterized as $sin(\theta)$. This directivity pattern is observed in the experimental findings. The spread in $\pm10°$ and $\pm170°$, at the dipole nulls, show some spread of the data which is attributed to the low signal to noise ratios at those angular positions. While the mean of the spread is consistent with the theoretical predictions at $\pm130°$, there also seems to be some noise at these angular positions. Lastly, the theoretical predictions under-estimate the radiated noise at $\pm40°$.

4.5 Source Waveforms

The aeroacoustic source waveform was estimated from the microphone measurements, using Equations 4.1 through 4.3. Equation 4.1, which is written in the form of the observer, shows the factors that contribute to the radiated pressure. The $1/4\pi r_i$ accounts for spherical spreading, $D_i(t - \frac{r_i}{c})$ the acoustic source strength, and $\beta(\theta_i)$ the directivity pattern; for a rigid impermeable plate, $\beta(\theta_i)$ is equal to $sin(\theta/2)$, and $sin(\theta)$ for a highly porous plate. The subscript i refers to the angular position, θ_i for the i^{th} microphone. Equation 4.2 solves 4.1 for D_i, the source waveform estimated from the i^{th} microphone. Using Equation 4.3 the source waveform estimated $D_{avg}(t)$ is computed as the average of the D_i estimates.

$$p_i(t) = \frac{1}{4\pi r_i}\, D_i(t - \frac{r_i}{c})\, \beta(\theta_i) \tag{4.1}$$

$$D_i(t) = \frac{4\pi r_i}{\beta(\theta_i)}\, p_i(t + \frac{r_i}{c}) \tag{4.2}$$

$$D_{avg}(t) = \frac{1}{N_{fmic}} \sum_{i=1}^{N_{fmic}} D_i(t) \tag{4.3}$$

The results for the source waveforms in time will now be discussed. For all the ensembled-averaged conditions $\pm 10°$ were not used in the estimate of D_{avg} due to low signal-to noise. Figure 4.6 a) show the results for the rigid impermeable plate, $\mu/k = 0$. The waveforms monotonically decay as the vortex ring speed is reduced from 81 m/s to 39 m/s. This is due to the reduced radiated sound from a vortex ring passing the edge as its speed is reduced. Additionally, it is noticeable the waveforms are elongated with decreasing vortex ring speed. This is associated to the longer interaction time between the vortex ring and plate.

The results from $\mu/k = 0.49$, are shown in Figure 4.6 b). Although the second null of the dipole develops at $mu/k = 0.49$, shown in Figure 3.7 b), $\pm 170°$ were included in the estimate of $D_{avg}(t)$ since their was sufficient signal-to-noise. The waveforms in Figure 4.6 b) are obviously different than those in 4.6 a). Here, it is noticeable the negative peak before the maximum positive is reduced. This suggest the introduction of porosity changes the behavior of source sound, $D_{avg}(t)$. Additionally, we observe a monotonic decay in amplitude as vortex ring speed is reduced and elongated time.

Figure 4.6 c) shows the results for $\mu/k = 3.10$. Since reductions in radiated sound at the second null become more significant, the signal to noise ratio at $\pm 170°$ begins to diminish. For this reason, and those mentioned previously, $\pm 170°$ & $\pm 10°$ were not used in the estimate of $D_{avg}(t)$. As before, the waveforms show a monotonic decay with vortex ring speed. Also, the waveform elongation due to the increased source interaction time is observed. The shape of the waveform appear similar to case b) which was attributed to the introduced porosity on the plate.

The results for $\mu/k = 58.9$, are shown in Figure 4.6 d). $\pm 170°$ & $\pm 10°$ were not used in the estimate of $D_{avg}(t)$ for reasons discussed in case c). The waveforms in case d) resemble similar shapes as in cases b) and c). Additionally, the elongation in waveforms with decreasing vortex ring speed is observed. However, the monotonic decay trend seen in the prior cases is partially observed. Here, 72 m/s and 60 m/s do not follow this trend. When compared to Figure 4.3 d) these ensembled-averaged conditions appear to produce less radiated noise than their neighboring ensembled-averaged conditions. The decrease in radiated noise at 72 m/s is also observed in Figure 4.3 b) at 74 m/s. This suggests that an artifact of the vortex ring generator at this condition may be responsible.

4.6 Nondimensionalized Source Waveforms

The results for nondimensionalizing the source waveforms will now be discussed. First D was computed as $D_{avg}(t)/U^{n/2}$ for each ensembled-averaged speed and normalized by $D/max(D)$ at each ensemble. Time was then nondimensionalized as $\tau = (t - t_c)(U/a)$, where t_c, the convection time of the ring from nozzle to above the edge. To determine t_c the linear fit, shown in Figure 4.1 to approximate vortex ring speed, was extrapolated to Z_p to approximate the convection time. The peaks of D waveforms were aligned in nondimensionalized time at $\tau = 0$. These results are shown in Figure 4.7.

For every case, the lowest ensembled-averaged condition exhibits signs of noise while the general waveform is conserved. It can also be observed that with an increasing μ/k the source waveform transitions from a sinusoidal "S" shape, as in case a), to the predicted "W" shape. This indicates the nearfield transparency effectively alters the generated noise at the source level. The average of these waveforms at every case a) through d) was taken as, $\bar{D}$, and plotted adjacent to the theoretical predictions of Chen et al.[1]. These results are shown in Figure 4.8.

It must be addressed that the computation of $\bar{D}$ and $\mathrm{D}_t^m[g(\bar{t})]$ are slightly varied. A more defined comparison, where the source waveforms from theory and experiment are being developed. Therefore, the only observations that can be made currently are in regards to waveform shape. It can be observed the experimentally computed waveforms are not as pronounced as the predicted. However, some trends are present. For the high μ/k waveforms, some symmetry is visible along with a more pronounced negative peak after $\tau = 0$. Additionally, in regards $\mu/k = 0$ it can be observed the negative curve of $\bar{D}$ before $\tau = 0$ and positive curve of $\bar{D}$ after $\tau = 0$ is a shared characteristic. Lastly, it can be observed that increasing μ/k effects of the source waveform for both instances.

4.7 Impact Distance Scaling

The effects of sound power scaling with impact distance L will now be discussed. These results are shown in Figure 4.9. As the radiated noise decreases with L the $\Delta p_i^2(\theta)$ for angles close to the nulls approach low signal to noise levels. Therefore, these θs have been omitted and only signals with high signal to noise ratios are reported, shown in Table 4.2. For $\mu/k = 0$ these include θ equal to $\pm 170°$ and $\pm 130°$, and for $\mu/k = 58.9$ $\pm 100°$ and $\pm 70°$. For $\mu/k = 0$, seen in Figure 4.9 a), the mean sound power scaled as $\bar{m} = -4.04$, or $\sim L^{-4}$ which corroborates near the predicted value of Kambe et al.[11] of L^{-4} and the experimental results of Kambe et al.[11] of $L^{-4.48}$. For $\mu/k = 58.9$, seen in Figure 4.9 b), the mean sound power scaling exponent is $\bar{m} = -4.94$, or $\sim L^{-5}$. These results are in agreement with the predictions of Chen et al.[1] as L^{-5}.

θ	m	R^2
-170	-4.21	0.9642
-130	-3.92	0.9787
130	-3.97	0.9923
170	-4.04	0.9871

(a) $mu/k = 0$

θ	m	R^2
-100	-4.88	0.9861
-70	-4.93	0.9388
70	-5.00	0.9798
100	-4.96	0.9736

(b) $mu/k = 58.9$

Table 4.2: Sound power scaling as a function of impact distance (L) where a) $\bar{m} = -4.04$ and b) $\bar{m} = -4.94$.

4.8 Discussion

4.8.1 Uncertainty and Error of Reported Quantities

The objective of this section is to overview the sources of uncertainty associated to the measured quantities used to compute the reported quantities, Δp, acoustic directivity, $\bar{n}$, $\bar{m}$, and source strength waveform. This effort helps to characterize confidence limits on the measurements presented herein, to help explain any discrepancies between theoretical prediction and measurement. The focus of the current discussion is on measurement uncertainty, with some discussion on how this affects uncertainty of reported quantities, which are not fully presented here.

The measured quantities that contribute to the uncertainty in the radiated sound from the vortex edge interaction, Δp, defined in Chapter 1, will be discussed first. These sources include inaccurate microphone position uncertainty in both radial distance from the edge and angular position θ. The resolution of these quantities were measured as $\pm 3mm$ and $\pm 5°$ for radial distance and angular position, respectively. In addition to microphone position, uncertainty in Δp could also arise from variations in the ensembled-average of the 5 vortex-edge interaction realizations. These realizations were grouped by vortex ring speed, U_R, where each realizations fell within $\pm 1m/s$ of the grouped mean. As discussed in Chapter 3.3.2, U_R was estimated from the high speed Schlieren. This process included a) tracking vortex ring position in each frame and b) applying a linear fit to the VR position vs time data to approximate U_R. Both of these steps propagate the measurement error to the estimate of Δp. Lastly, vortex ring path variability during its convection past the plate edge contributes to greater uncertainty in the ensemble average of both vortex ring speed U_R and radiated sound Δp. Since it has been shown changes in L impact the amplitude of the radiated noise from the vortex plate edge interaction, i.e. $\bar{m}$, the collection of data was controlled such that the VR convection path was at the appropriate L.

The uncertainty in the reported acoustic directivity $\beta(\theta)$ comes from measurement uncertainty in both Δp and microphone position. These sources were quantified and discussed in the previous paragraph.

The measured quantities U_R and Δ_p also influence the uncertainty in the reported power law exponent $\bar{n}$. The uncertainty in these quantities propagates through the power law fit used to estimate $\bar{n}$. In addition, for each plate a nominal mean μ/k is reported. For the cases of $\mu/k = 0.49$ and $\mu/k = 3.10$, $\bar{n}$ is a strong function of μ/k. Because μ/k depends on vortex ring speed, and because we estimate n using a power law fit of Δp vs. U_R, the variation in μ/k inherent in this approach can contribute additional uncertainty to the $\bar{n}$ estimate.

The final reported variable that has potential sources of error is source strength D_i, described in Equation 4.2. Measured quantities with potential error that influence this variable include $\beta(\theta)$, r_i, c, and $p_i(t)$, where $\beta(\theta)$ and r_i have previously been discussed. Since there is a temporal dependency to calculate the source waveform, the propagation time r/c from the source to each receiver is required. Variables that influence the propagation time uncertainty are a) the uncertainty in the radial distance of the microphone and b) uncertainty in the speed of sound. As discussed previously the radial distance r_i uncertainty was $\pm 3mm$. The ambient temperature, required to compute the speed of sound c, was acquired with a

Fluke 80TK thermocouple which had a resolution of $\pm 0.1°C$. Considering radial distance variations only, the propagation time uncertainty was $\pm 8.8 \mu sec$. When compared to the sample rate of the data acquisition system of 51.2kHz, or a sample every $19.5 \mu sec$, the propagation time uncertainty is approximately ± 0.45 samples. Uncertainties in both speed of sound and microphone thus contribute to $D_{avg}(t)$ uncertainty directly through the estimated propagation time. Propagation time uncertainty also contributes to $D_{avg}(t)$ uncertainty during the ensemble averaging step, due to phase misalignment of the individual realizations. This uncertainty is more in the form of a bias error which can be corrected for, as discussed above.

4.8.2 Implications for Owl Foraging Behavior

In this idealised trailing edge noise study it has been observed that increases in μ/k, i.e. porosity, have correlated with reductions in trailing edge noise. However, the connection between this result, the previously reported literature, and the implications it has on owl foraging behavior remains lacking. Therefore, an overview of how others have used aeroacoustic theory to work out the connection between owl wing TE sound generation and owl wing morphology will first be discussed. Then an explanation on how owls are able to benefit from the reduced TE noise, in regard to their foraging behaviors, will be addressed for both large and small owl species. In this way, the discussion will establish a bridge between the results from the vortex plate experiment and how they are reflected in the quiet flight of owls.

The development of aeroacoustic theory to define the sound generated by owl wings and owl wing morphology is summarized in an annual review by Jaworski and Peake[47]. This work encompasses a review of characteristics related to owl wing morphology like surface roughness, leading edge serrations, and fringe, but this discussion will only focus on the section related to the porous features along the owl wing trailing edge plumage. The authors show a) how the turbulent boundary layer development on the owl wing is responsible for the TE edge noise, b) the theoretical predictions and methods to estimate radiate TE noise[33;34;1] and c) examine the trailing edge aeroacoustic behavior associated to both large and small wing morphologies. Their examination on a diverse population of owl species introduces quantifiable evidence that shows wide variations in owl wing morphology based on owl size. Notably, these findings show for large owl species the chord lengths are large, whereas they are small for smaller owl species. For small owl species with reduced chord lengths, a turbulent boundary layer does not develop, and as a result any porosity near the trailing edge plumage does not attenuate TE noise, since it is lacking. For large owl species, the chord lengths are adequate for a turbulent boundary layer to develop. Therefore, it has been hypothesized porous features in the trailing edge plumage, along with elasticity, can attenuate the TE noise source.[33;34;1;47] However empirical evidence to support these speculations has remained unwarranted. The contributions from this research fills a partial element of this speculation by showing reductions in trailing edge noise are achievable with increasing porosity – assuming the turbulent boundary layer develops on the wing.

In addition to a reduction in the amplitude of radiated noise from the trailing edge noise source, the porous elements along the trailing edge plumage suppress the directionality of the TE noise source. In Chapter 4.4 it was shown increases in μ/k lead to an acoustic directivity transition from cardioid to dipole for low to high μ/k values, respectively. Assuming $\mu/k \gg 1$ for large owl species wings, the directionality of their TE noise would radiate largely on the suction and pressure sides of their winged lifting surfaces and emit less noise than a rigid impermeable wing type. An obvious observation when comparing the results from this experiment to the forward flight of owls in the angle of the turbulent eddy convection pathway. For the reported experiment all vortex rings were controlled to convect normal to the plate surface at offset distance L. Theoretical work by Kambe et al.[11] and Chen et al.[1], for rigid impermeable and rigid porous, respectively, investigated the impact of changes in this angle had in relationship to the radiated noise directivity, i.e convection angles typical for lifting surfaces in forward flight. Their findings showed the cardioid and dipole lobes were unchanged when the angle of the convection path of the eddy changed, meaning the directivity of the vortex plate edge experiment is comparable to the forward flight of large owl species.

Simply put, how do owl species benefit from this TE noise suppression. An answer to this question requires a little background and understanding of the foraging behaviors of owls. For smaller species, like the elf and northern pygmy who feed upon small insects with a pounce-like lunge to grab prey, there is no benefit since the no trailing edge noise develops. For larger species, like the great horned or snowy owls, who feed upon small mammals like voles and mice with a glide-approach, the porous features along the trailing edge plumage are more significant to reduce TE noise. Apart from attenuating the TE noise amplitude, an additional benefit of this suppression is associated to the frequencies where the attenuation occurs. As discussed in Chapter 1, Lilley[21] and Jaworki and Peake[47] showed this attenuation occurs in frequency ranges $\sim 1-2kHz$, which is a frequency band sensitive to the hearing of their prey. Lastly, the transition from cardioid to dipole, for porous lifting sources, could also act as a benefit to owls that utilize a glide-approach to their prey. With porous elements along the trailing edge plumage, the directionality of the TE noise is reduced in the forward direction. This means as an owl glides towards its prey, they prey is more susceptible since it will detect the acoustic signature of the owl at a delayed time – reducing reaction time.

From the empirical support of the results in this experiment it was shown the theory is broadly correct. Therefore, to enhance the understanding of the aeroacoustic behavior of the large owl species a study that precisely characterizes owl wing morphology in terms of μ/k is logical. Additionally, this investigation would be a prime opportunity to support future works that investigate the theoretical predictions for reductions in radiated noise from TE noise sources for poro-elastic wing types.

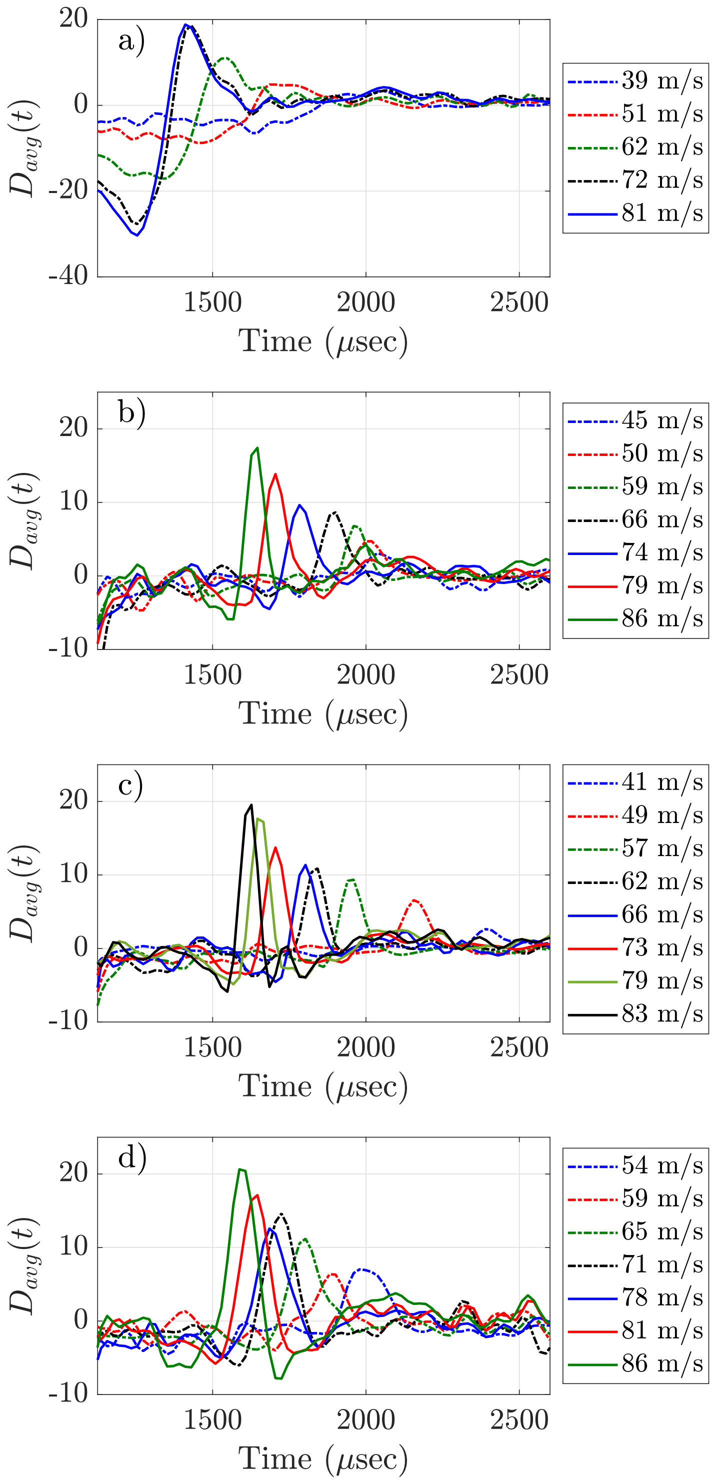

Figure 4.6: Averaged source waveforms, $D_{t_{avg}}(t)$, for (a) $\mu/k = 0$, (b) $\mu/k = 0.49$, (c) $\mu/k = 3.10$, and (d) $\mu/k = 58.9$. Line color and type indicate vortex ring speed shown in legends.

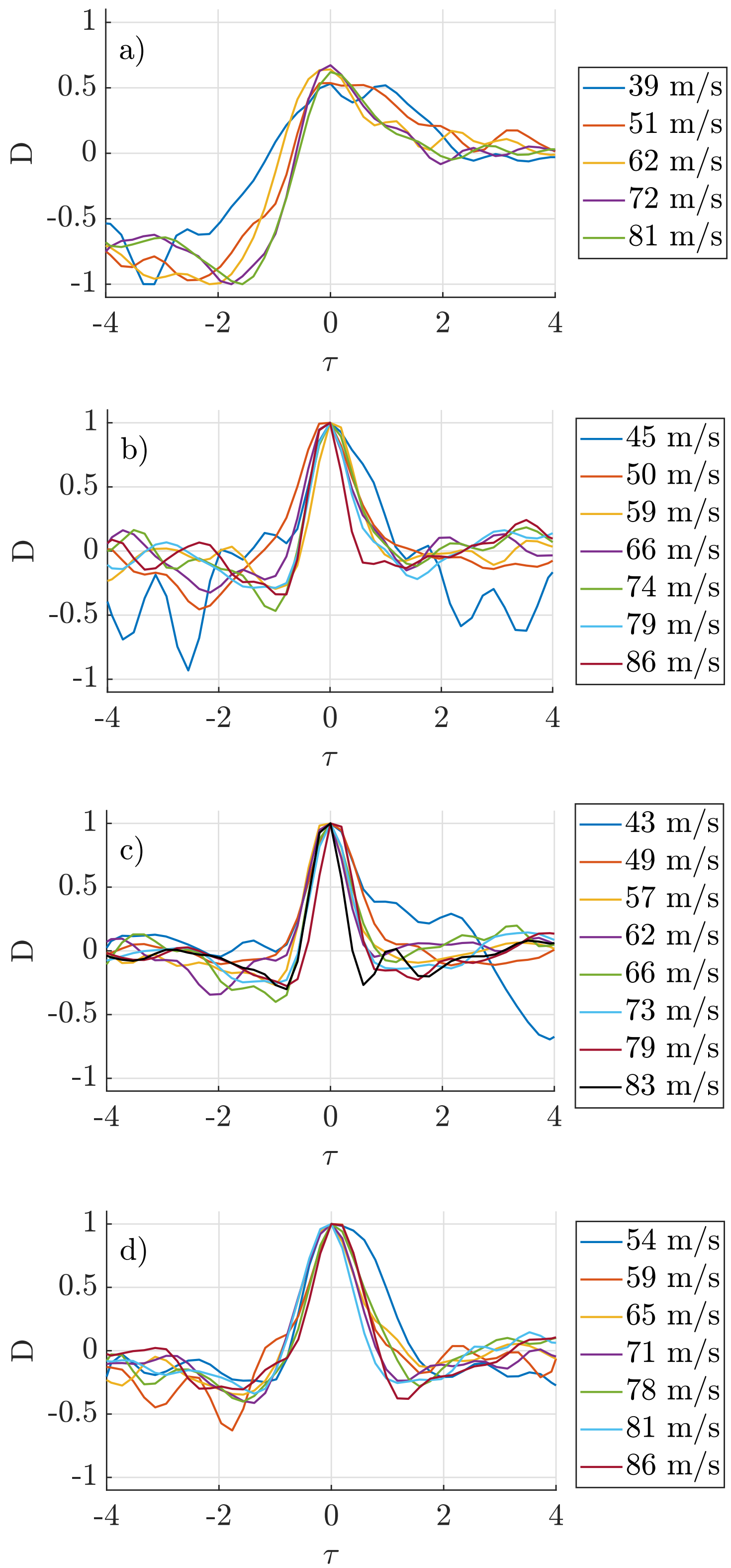

Figure 4.7: Nondimensionalized source waveforms, D, versus nondimensionalized time, τ for (a) $\mu/k = 0$, (b) $\mu/k = 0.49$, (c) $\mu/k = 3.10$, and (d) $\mu/k = 58.9$. Line color and type indicate vortex ring speed shown in legends.

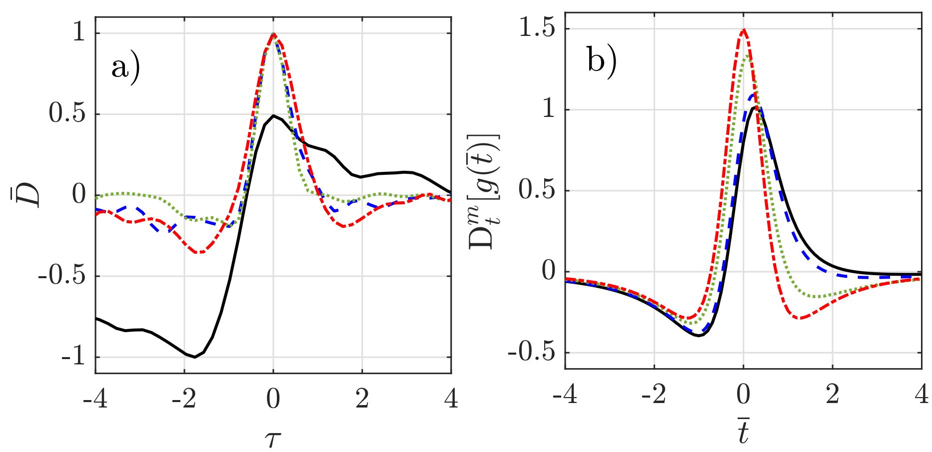

Figure 4.8: Comparison of experimentally computed $\bar{D}$, a), to predicted nondimensionalized source waveforms from Chen et al[1], b). For a) -, –, :, and -. represent $\mu/k = 0$, 0.49, 3.10, and 58.9, respectively. For b) -, –, :, and -. represent $\mu/k \leq O(10^{-2})$, 0.2, 1, and $\geq O(10)$, respectively.

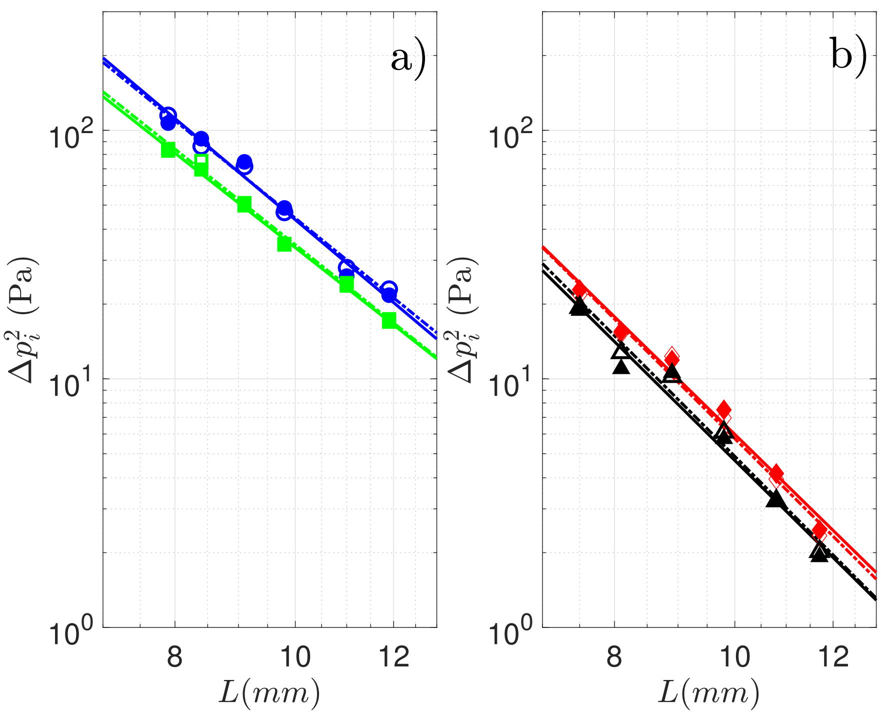

Figure 4.9: Sound power (Δp_i^2) as a function of impact distance L. Subplot a) $\mu/k = 0$ and the ○ and □ represent ±170° and ±130°, respectively. Unfilled shapes correspond to positive values of θ. The solid(-) and dashed(- -) lines correspond to the power-fit performed on negative and positive θs respectively. Subplot (b) $\mu/k = 58.9$ and the ◇ and △ represent ±100° and ±70°, respectively. The same line notation is used as in subplot a).

Chapter 5

Conclusions

5.1 Contributions

This thesis has investigated the impact that porosity has on the behavior of the radiated noise from a turbulent eddy convecting near the edge of a non-compact rigid porous plate. The primary goal was to provide validation to the theoretical predictions of Jaworski and Peake[33], Cavalieri et al.[34] and Chen et al.[1]. Specific contributions of this work include:

1. Demonstrated the effectiveness of acquiring measurements in an anechoic chamber, rather than a wind-tunnel, which had previously shown to be unsuccessful.

2. Measurements were performed for a vortex ring convecting past the edge of a non-compact plate. Sound source waveform, directivity, and the power law relation between sound power and characteristic source speed, on one hand, and sound power and impact distance, on the other, were estimated from the measurements.

3. Comparison of predictions of these quantities showed:

   (a) Good agreement for the sound power-ring speed power law

   (b) Good agreement for the sound power-impact distance power law.

   (c) Qualitative agreement between acoustic directivity - while measurement showed a skewed-lobe dipole pattern, where the skewing decreased with porosity, the degree of skewing was over-predicted.

(d) Qualitative agreement in shape of source waveforms – similar to directivity, predicted trends were observed but the degree of change with porosity was over-predicted.

5.2 Recommendations for Future Work

There are many means to extend this work in future investigations. Foremost, the scope of this thesis focused on uniformly distributed porosity on the plates, which corresponded to the claims made by Jaworski and Peake[33] Cavalieri et al.[34], and Chen et al.[1]. Future experimental work should consider the effects of finite spans of porosity along the lifting surface. Additionally, Jaworski and Peake[33] Cavalieri et al.[34] also identify parametric ranges for reductions in TE noise with elastic and poro-elastic plates. For the elastic condition it could be determined how the sound power laws and source waveforms change with increasing elasticity. Then a combination of uniform poro-elastic and finite poro-elastic could be considered. These methods seem readily adaptable to the vortex ring / plate experimental setup presented. However, these predictions suggest potential for U^7 sound power scaling which may be difficult to capture as the signal to noise ratio is reduced, especially for microphones near the nulls of the dipole.

The discussed vortex ring / plate experiment is a simplified case of TE noise that corresponds to a single eddy convecting near the plate. An experiment that would determine the efficiency and effectiveness of porous, elastic, and poro-elastic treatments for more applicable lifting surfaces could be performed with a glider. Equipping the glider with the aforementioned airfoils and collecting a) radiated noise measurements with on-board and fly over microphones and b) vehicle sensors such as a pitot tube, 3 axis accelerometers, and pressure transducers would determine the aeroacoustic vs aerodynamic consequences of porous lifting surface treatments.

Appendix
Post Processing Matlab Scripts

This appendix shows the scripts used in the analysis of the vortex ring interacting with an edge study. The acoustic data is first analyzed followed by the image processing to approximate U_R.

```
clc
clear
close all

%% Analysis

% The puropose of this script is to analyze the results taken from the
% vortex plate experiment. The experiment entails convecting a vortex ring
% near plate, which varied from a rigid impermeable plate to plates that
% increased in \mu/k (see Jaworski and Peake 2013).

% The script takes data (pre-sorted for user convenience) and loads it in
% based upon the plate type. Select a plate type here....

impermeable=1;
rigid_porous_plate_2 =0;
rigid_porous_plate_3 =0;
rigid_porous_plate_4 =0;
```

```
% This will open the file directory to access that plate data. Within these
% directories are the VR speeds tested, and a file within there has all of
% the paths to access the 5x data files that comprise the 5x ensemble
% average. These will be loaded in as Data.Case(ii) where ii = the number
% of speeds tested on that plate. Data is a full structure with appropriate
% headers for all the individual raw tests, the ensembled, the ensembled
% filtered, etc.

%Author: Zachary Yoas
%Date: 4/28/2021

%% Preallocating (Constants, Experimental Parameters, etc)

mic_chan_leg = ["-170\circ", "-130\circ","-100\circ","  -70\circ",...
"  -40\circ"," -10\circ","  10\circ","   40\circ","   70\circ",...
" 100\circ"," 130\circ"," 170\circ"].';
mic_num_deg = [-170, -130, -100, -70, -40, -10, 10, 40, 70, 100, 130, 170];
mic_num_rad = zeros(1,length(mic_num_deg));
mic_radius = [.5 .5 .5 .5 .5 .5 .5 .5 .5 .5 .5 .5]; %Mic distances
space = ' ';

%Converting degrees to radians for directivity plots
for ii=1:length(mic_num_deg)
mic_num_rad(1,ii) = (mic_num_deg(ii)*(pi/180));
end

%Loading in theoretical directivity measurements
load('beta_rs.mat')
load('directivity_theory.mat')

% Using cmap for color order
cmap = colormap(brewermap([],'Set1'));
```

```
close

%Marker Loops
markers = {'o','s','d','^','v','>','>','v','^','d','s','o'};
marker_fill = {'b','g','r','k','m','c','none','none','none',...
        'none','none','none'};
colors = {'b','g','r','k','m','c','c','m','k','r','g','b'};
linestyle = {'none'};
line_style ={'-','-','-','-','-','-','-.','-.','-.','-.','-.','-.'};

%To circulate markers, include this portion below.
getFirst = @(v)v{1};
getprop = @(options, idx)getFirst(circshift(options,-idx+1));

%% User selects the plots to view

plot_nondim_directivity =1;
plot_pwaveform =0;
plot_dwaveform = 0;
plot_davg =1;
plot_nondim_davg = 1;

%Saving loop
save = 0;


%% Plate Parameters
% This part of the script is very sensitive, please avoid adjusting.
% Once the user defines the plate type, the parameters given
% below are the speeds in the Data sub folder for that plate type.

if impermeable ==1
speeds=[39 47 62 72 81];% VR speeds
```

```
L = [47 47 54 54 54];
mic_select = [1 2 3 4 5 8 9 10 11 12];
%mics 6-7 not included (low sig/noise).
end

if rigid_porous_plate_2 ==1
speeds=[45 50 58 66 73 79 86];
mic_select=[1 2 3 4 5 8 9 10 11 12];
end

if rigid_porous_plate_3 ==1
speeds=[40 50 56 62 67 73 79 84];
mic_select=[1 2 3 4 5 8 9 10 11 12];
end

if rigid_porous_plate_4 ==1
speeds=[54 60 65 72 78 82 86];
mic_select=[1 2 3 4 5 8 9 10 11 12];
end

%% Loading in data for plate condition

%Preallocating the data structure. This will hold ALL data
Data = struct();
if impermeable ==1

%loads in data via path and is assigned to Data
%structure as a CASE(ii)
for ii = 1:length(speeds)
temp01 = %% Folder path %%
temp02 = %% File path %%
baseName_data = (temp01);
folder_data = (temp02);
```

```
load(temp02)
Data.Case(ii) = Summary;
end
end

if rigid_porous_plate_2 ==1
for ii = 1:length(speeds)
temp01 = %% Folder path %%
temp02 = %% File path %%
baseName_data = (temp01);
folder_data = (temp02);
load(temp02)
Data.Case(ii) = Summary;
end
end

if rigid_porous_plate_3 ==1
for ii = 1:length(speeds)
temp01 = %% Folder path %%
temp02 = %% File path %%        baseName_data = (temp01);
folder_data = (temp02);
load(temp02)
Data.Case(ii) = Summary;
end
end

if rigid_porous_plate_4 ==1
for ii = 1:length(speeds)
temp01 = %% Folder path %%
temp02 = %% File path %%        baseName_data = (temp01);
folder_data = (temp02);
load(temp02)
Data.Case(ii) = Summary;
```

```
end
end

%preallocate
temp = {};

%Extract the mean VR speed from the HSV data
for ii = 1:length(speeds)
speeds_v2(ii) = mean([Data.Case(ii).VR_HSV_VR(:).Ring_Speed]);
temp(ii) = strcat(num2str(round(speeds_v2(ii))),{' '},'m/s');
end

%This builds a legend for the cases that will be used later
leg_build = temp;


%% Constraining data series to trigger impulse

for ii=1:length(speeds_v2)
for jj = 1:12
[min_PP_pa,min_PP_index] = ...
min(abs(Data.Case(ii).VR_time_array(1,:))); %find the 0 point
Data.Case(ii).VR_sig(:,jj) = Data.Case(ii).VR_ensembled_signal_filt...
(min_PP_index+mic_distance_correction(jj):min_PP_index+...
mic_distance_correction(jj)+299,jj);
end
end

%% Powerfit

% get delta p for mic (number) for all the cases
for ii = 1:length(speeds)
delta_p(1:12,ii) = Data.Case(ii).VR_delta_p(:);
```

```
end

% And now again for the negative degree angles
count = 6:18;
expon_str =string();
count02 = [1:length(mic_select)];
count03 = 1;

% Using the delta_ps and speeds from the cases we can ...
% find a power fit in the form
% (b*x^m) for every microphone

%%%%%%%%%%%% %Plotting powerfit data
figure(1)
for ii=mic_select
[p,S] = polyfit(log(speeds_v2),log((delta_p(ii,:).^2)),1);...
%this is the power fit
m = p(1); %this is the exponent
k(count03) = m; %stores "n" for each microphone
q(count03) = exp(p(2));

temp = num2str(num2str(round(m,2)));
expon_str(ii) = strcat(mic_chan_leg(ii),{' '},{' '},...
num2str(round(m,2)));
expon_str(ii) = strcat(expon_str(ii));
b = exp(p(2));
a = fplot(@(speeds_v2) b*(speeds_v2).^m,[speeds_v2(1)-4 ...
speeds_v2(end)+10]...
,'LineStyle','-.','LineWidth',2,'HandleVisibility','off');
hold on
set(a,'color',getprop(colors,ii))
set(a,'LineStyle',getprop(line_style,ii),'LineWidth',1.5)
set(a,'DisplayName',expon_str(ii))
```

```
hold on
R_2(ii) = 1-(S.normr/norm(delta_p(ii,:) - mean(delta_p(ii,:))))^2;
legend ('Location','eastoutside')
count03 = count03 +1;
end
%%%%%%%%%%

%% Plotting Pa vs U
plot(0,0,'DisplayName','    \theta       n','Marker',...
'none','Color','none')
hold on
for jj=mic_select
plot(speeds_v2(:),(delta_p(jj,:).^2),'DisplayName',expon_str(jj),...
'Marker',getprop(markers,jj),'MarkerSize',10,'color',...
getprop(colors,jj),'MarkerFaceColor',getprop(marker_fill,jj),...
'linestyle','none','HandleVisibility','on')
hold on
grid on
set(gca,'xscale','log','yscale','log')
legend ('Location','eastoutside')
end

grid on
xmin = floor(min(speeds))-5; %show xlim at U_R slightly below...
%last VR condition
xmax = ceil(max(speeds))+ 5;
xlim([xmin xmax])
%     ylim([.25 10])
ylabel('$\Delta p_{i}^2$ (Pa)','Interpreter','Latex','FontSize',16)
xlabel('$U_{R} (m/s)$','Interpreter','Latex','FontSize',16)
set(gca,'FontSize',16)
set(gcf, 'Position',  [100, 100, 500, 400])
sdf(1,'Thesis')
```

```
temp = strcat('Radiated Sound Power Scaling');

if save == 1
temp03 = folder_data(1:end-17);
save_name = strcat(temp03,'Radiated Sound Power Scaling');
saveas(figure(1),save_name,'fig')
saveas(figure(1),save_name,'png')
end


%% n bar
nbar = mean(k);

%% Calculating Normalized Delta P
non_dim_p = zeros(size(delta_p)); %preallocating

% Calculating normalized delta p
if impermeable == 1
for ii = 1:length(speeds_v2)
for jj=mic_select
non_dim_p(jj,ii) = abs(delta_p(jj,ii)./beta_rs(jj,1));
end
end
non_dim_p_wo_zero_rows = non_dim_p(any(non_dim_p,2),:);
%removes 0 rows
end

if rigid_porous_plate_2
for ii = 1:length(speeds_v2)
for jj=mic_select
non_dim_p(jj,ii) = abs(delta_p(jj,ii)./beta_rs(jj,2));
end
end
```

```
non_dim_p_wo_zero_rows = non_dim_p(any(non_dim_p,2),:);
%removes 0 rows
end

if rigid_porous_plate_3
for ii = 1:length(speeds_v2)
for jj=mic_select
non_dim_p(jj,ii) = abs(delta_p(jj,ii)./beta_rs(jj,3));
end
end
non_dim_p_wo_zero_rows = non_dim_p(any(non_dim_p,2),:);
%removes 0 rows
end

if rigid_porous_plate_4
for ii = 1:length(speeds_v2)
for jj=mic_select
non_dim_p(jj,ii) = abs(delta_p(jj,ii)./beta_rs(jj,4));
end
end
non_dim_p_wo_zero_rows = non_dim_p(any(non_dim_p,2),:);
%removes 0 rows
end

% Normalized Directivity using mean exponent value
if plot_nondim_directivity == 1
non_dim_p = struct();

for ii =1:length(speeds)
for jj = 1:12
non_dim_p.case(ii).del_p(jj,1) = ...
Data.Case(ii).VR_delta_p(jj,1);
non_dim_p.case(ii).del_p(jj,1) = non_dim_p.case(ii).del_p(jj,1)...
```

```
/((speeds_v2(ii).^nbar));
end
end


%find max at each +/- (angle) and averaging to normalize to 1
%by taking average of +/- this accounts for noise.
for ii=1:length(speeds_v2)
avg_delp(1) = (non_dim_p.case(ii).del_p(1) + ...
(non_dim_p.case(ii).del_p(12)))/2; % gives mean between ...
%=+/- 170 deg to get normalizations
avg_delp(2) = (non_dim_p.case(ii).del_p(2) + ...
(non_dim_p.case(ii).del_p(11)))/2; % gives mean between ...
=+/- 130 deg to get normalizations
avg_delp(3) = (non_dim_p.case(ii).del_p(3) + ...
(non_dim_p.case(ii).del_p(10)))/2; % gives mean between ...
%=+/- 100 deg to get normalizations
avg_delp(4) = (non_dim_p.case(ii).del_p(4) + ...
(non_dim_p.case(ii).del_p(9)))/2; % gives mean between ...
%=+/- 70 deg to get normalizations
avg_delp(5) = (non_dim_p.case(ii).del_p(5) + ...
(non_dim_p.case(ii).del_p(8)))/2; % gives mean between ....
%=+/- 40 deg to get normalizations
avg_delp(6) = (non_dim_p.case(ii).del_p(6) + ...
(non_dim_p.case(ii).del_p(7)))/2; % gives mean between ...
% =+/- 10 deg to get normalizations
norm(ii) = max(avg_delp);
end

%Normalize to 1 nondimensional directivity plot
for ii=1:length(speeds_v2)
non_dim_p_normalized(:,ii) = non_dim_p.case(ii).del_p/norm(ii);
end
```

```
%Plotting normalized directivity
figure(2)
for ii=1:length(speeds)
polarplot(mic_num_rad,non_dim_p_normalized(:,ii),...
'MarkerSize',9,'Marker',getprop(markers,ii),...
'LineStyle','none','Markerfacecolor',cmap(ii,:),...
'Color',cmap(ii,:))
hold on
thetaticks([10 40 70 100 130 170 190 230 260 290 320 350])
thetaticklabels({'10','40','70','100', '130','170',...
        '-170', '-130','-100','-70','-40','-10'})
end
legend(leg_build)

%Overlaying theoretical directivity curve
if impermeable == 1
polarplot(directivty1(:,1),directivty1(:,2),'-',...
'Color','black','LineWidth',2,'HandleVisibility','off')
end

if rigid_porous_plate_2 ==1
polarplot(directivty2(:,1),directivty2(:,2),'-',...
'Color','black','LineWidth',2,'HandleVisibility','off')
end

if rigid_porous_plate_3 ==1
polarplot(directivty3(:,1),directivty3(:,2),'-',...
'Color','black','LineWidth',2,'HandleVisibility','off')
end

if rigid_porous_plate_4 == 1
polarplot(directivty4(:,1),directivty4(:,2),'-',...
```

```
'Color','black','LineWidth',2,'HandleVisibility','off')
end

rlim([0 1.2])

if save == 1
temp03 = folder_data(1:end-17);
save_name = strcat(temp03,'Normalized Pressure');
saveas(figure(2),save_name,'fig')
saveas(figure(2),save_name,'png')
end
end

%% Pwaveforms

%Here we plot the microphone ensembled conditions
count01 = [12 11 10 9 8 7];

%Plotting the first six microphones (1-6) is (-170, -130, -100....)
%respectively.
if plot_pwaveform==1
for ii=1:length(speeds_v2)
for jj = 1:6
figure(200+ii)
subplot(2,1,1)
plot(time,Data.Case(ii).VR_sig(:,jj),'LineWidth',1.5,...
'DisplayName',mic_chan_leg(jj))
hold on
legend('Location','eastoutside','FontSize',13)
grid on
xlim([1100 2200])
ylabel('$P_i$ (Pa)','Interpreter','Latex','FontSize',16)
xlabel('Time ($\mu$sec)','Interpreter','Latex','FontSize',16)
```

```
ylim([-7 7])
end

%Plotting the first six microphones (7-12) is (10, 40, 70, 100....)
%respectively.
for jj=1:6
figure(200+ii)
subplot(2,1,2)
plot(time,Data.Case(ii).VR_sig(:,count01(jj)),'LineWidth',...
1.5,'DisplayName',mic_chan_leg(count01(jj)))
hold on
legend('Location','eastoutside','FontSize',13)
grid on
xlim([1100 2200])
ylim([-7 7])
ylabel('$P_i$ (Pa)','Interpreter','Latex','FontSize',16)
xlabel('Time ($\mu$sec)','Interpreter','Latex','FontSize',16)
end
end
end

%% Source Waveform (Dt_i)

% p_i = 1/(4*pi*r) * B(\theta)* D(t)
% D_i = ((4*pi*r)(p)) / B(\theta)  <--- this rearrangment gets ...
% back to source waveform (MHK)

% The experimental directivity is used
% in the computation of D_i

B_theta = zeros(12,1); %preallocating

for ii = 1:12 %because 12 microphones
```

```
B_theta(ii) = mean(non_dim_p_normalized(ii,:));
end

%Calculating D_i
for ii=1:length(speeds)
for jj=1:12
Data.Case(ii).D_i(:,jj) = ((4*pi*mic_radius(jj))*...
Data.Case(ii).VR_sig(:,jj))/(B_theta(jj));
end
end

%Plotting D_i(t)
if plot_dwaveform ==1
for ii=1:length(speeds_v2)
for jj=1:12
if jj<7
figure(300+ii)
subplot(2,1,1)
plot(time,Data.Case(ii).D_i(:,jj),'DisplayName',...
strcat(num2str(mic_num_deg(jj)),'^{\circ}'),...
'LineWidth',1.5)
hold on
elseif  jj>6
subplot(2,1,2)
plot(time,Data.Case(ii).D_i(:,jj),'DisplayName',...
strcat(num2str(mic_num_deg(jj)),'^{\circ}'),...
'LineWidth',1.5)
hold on
end
grid on
legend('Location','eastoutside')
ylabel('$D_i(t) = (4*\pi*r_i)/\beta(\theta)$)',...
'Interpreter','Latex','FontSize',16)
```

```
xlabel('Time ($\mu$sec)','Interpreter','Latex','FontSize',16)
xlim([1100 2100])
end


if save == 1
temp = strcat('D_i_t',{' '},leg_build(ii));
temp03 = folder_data(1:end-17);
save_name = strcat(temp03,temp);
saveas(figure(200+ii),save_name,'fig')
saveas(figure(200+ii),save_name,'png')
end
end
end



%% Calculating D_avg(t)
%D(t) = 1/N sum(Dt_i(:,ii))

%Exclude measurements mentioned below for low S/N ratios
%For rigid imperm (exclude 10 and -10 degree measurements)
%For rigid_porous_plate_2 (exclude 10 and -10 degree measurements)
%For rigid_porous_plate_3 (exclude 10 and -10 degree and...
%-170 and 170 degree measurements)
%For rigid_porous_plate_3 (exclude 10 and -10 degree and...
%-170 and 170 degree measurements)

if impermeable ==1
for ii = 1:length(speeds_v2)
for jj=1:length(Data.Case(ii).D_i)
Dt_avg_neg_theta(jj,1) = -1.*sum(Data.Case(ii).D_i(jj,1:5))/6;...
%steps through each time step (jj) and takes average
```

```
Dt_avg_pos_theta(jj,1) = sum(Data.Case(ii).D_i(jj,8:12))/6;
Data.Case(ii).Dt_avg(jj,1) = sum(Dt_avg_neg_theta(jj)+...
Dt_avg_pos_theta(jj))/2;
end
end
end

if rigid_porous_plate_2 ==1
for ii = 1:length(speeds_v2)
for jj=1:length(Data.Case(ii).D_i)
Dt_avg_neg_theta(jj,1) = -1.*sum(Data.Case(ii).D_i(jj,2:5))/5;...
%steps through each time step (jj) and takes average
Dt_avg_pos_theta(jj,1) = sum(Data.Case(ii).D_i(jj,8:11))/5;
Data.Case(ii).Dt_avg(jj,1) = sum(Dt_avg_neg_theta(jj)+...
Dt_avg_pos_theta(jj))/2;
end
end
end

if rigid_porous_plate_3 ==1
for ii = 1:length(speeds_v2)
for jj=1:length(Data.Case(ii).D_i)
Dt_avg_neg_theta(jj,1) = -1.*sum(Data.Case(ii).D_i(jj,2:5))...
/5; %steps through each time step (jj) and takes average
Dt_avg_pos_theta(jj,1) = sum(Data.Case(ii).D_i(jj,8:11))/5;
Data.Case(ii).Dt_avg(jj,1) = sum(Dt_avg_neg_theta(jj)+...
Dt_avg_pos_theta(jj))/2;
end
end
end

if rigid_porous_plate_4 ==1
for ii = 1:length(speeds_v2)
```

```
for jj=1:length(Data.Case(ii).D_i)
Dt_avg_neg_theta(jj,1) = -1.*sum(Data.Case(ii).D_i(jj,2:5))...
/4; %steps through each time step (jj) and takes average
Dt_avg_pos_theta(jj,1) = sum(Data.Case(ii).D_i(jj,8:11))/4;
Data.Case(ii).Dt_avg(jj,1) = sum(Dt_avg_neg_theta(jj)+...
Dt_avg_pos_theta(jj))/2;
end
end
end

%Plotting D_avg
if plot_davg ==1
figure(400)
for ii=1:length(speeds_v2)
plot(time,Data.Case(ii).Dt_avg,'LineWidth',1.5)
hold on
end
grid on
ylabel('$D_{avg} (t)$','Interpreter','Latex','FontSize',16)
xlabel('Time ($\mu$sec)','Interpreter','Latex','FontSize',16)
xlim([1100 2600])
set(gca, 'fontsize',16)
end

%% Nondimesionalize D_bar and \tau
%convections times extracted from HSV for each ensemble

tc = Data.linearfit.tc(:); %pull the convection times acquired by ...
linear fit,VR x vs t.
tc = tc.*1e6; %because time is in microseconds
time_davg = time;

%Nondimensionalize Time (t - t_c) (U/ a)
```

```
for ii=1:length(speeds_v2)
nondimensional_time(:,ii) = (time_davg(1,:) -   tc(ii)) .*...
(speeds_v2(ii)/0.0065);
end

%Dt_avg / U^\nbar
%Normalize to 1
for ii=1:length(speeds_v2)
D_nondim(:,ii) = Data.Case(ii).Dt_avg/speeds_v2(ii)^(nbar/2);
max_val(ii) = max(D_nondim(:,ii));
D_nondim(:,ii) = D_nondim(:,ii)/max_val(ii);
end

% Align by (max positive peak)
% Need to constrain signal because max is being identified as S1

% Beginning index for constrain
if impermeable ==1
start_1 = 50;
else
start_1 = 60;
end

% Take constrain point and next 150 data points
% This is approximately 3000usec total
for ii=1:length(speeds_v2)
Data.Case(ii).Dt_avg_constrained = Data.Case(ii).Dt_avg(start_1:150,1);
end

%Dt_avg / U^\nbar
%Normalize to 1
for ii=1:length(speeds_v2)
D_nondim_constrained(:,ii) = Data.Case(ii).Dt_avg_constrained/...
```

```
speeds_v2(ii)^(nbar/2);
max_val(ii) = max(abs(D_nondim_constrained(:,ii)));
D_nondim_constrained(:,ii) = D_nondim_constrained(:,ii)/max_val(ii);
end

% Since the signal was constrained, we also constrain time, respectively.
time_davg = time(1,start_1:150);

%Find index for max positive peak
for ii=1:length(speeds_v2)
[max_davg(ii), max_davg_index(ii)] = max(D_nondim_constrained(:,ii));
end

%Create new time array
for ii=1:length(speeds_v2)
time_davg_shift(:,ii) = time_davg - time_davg(max_davg_index(ii));
end

% Plotting D_avg nondim
figure(600)
for ii=1:length(speeds_v2)
plot(time_davg_shift(:,ii),D_nondim_constrained(:,ii),'LineWidth',1.5)
hold on
end
grid on
ylabel('$D_{avg} (t) / U^{\bar{n}}$','Interpreter','Latex','FontSize',16)
xlabel('$(t - t_c)\frac{U}{a}$','Interpreter','Latex','FontSize',16)
xlabel('$\tau$','Interpreter','Latex','FontSize',16)
xlim([-4 4])
set(gca, 'fontsize',16)

% Here we calculate D_bar

```

```
        %Taking the mean D_avg at every time step
        for ii=2:length(D_avg_mean_waveform(:,1))
        D_mean(ii) = mean(D_non_dim_constrained(ii,:));
        end


        figure(700)
        plot(time_davg_shift(:,1),D_mean,'-k','LineWidth',1.5)
        grid on
        ylabel('$\bar{D}/ U^{\bar{n}}$','Interpreter','Latex','FontSize',16)
        xlabel('$(t - t_c)\frac{U}{a}$','Interpreter',...
        'Latex','FontSize',16)
        xlabel('$\tau$','Interpreter','Latex','FontSize',16)
        xlim([-4 4])
        set(gca, 'fontsize',16)

        %%%%%
        %%%%%
        %%%%%
        %%%%%
        %%%%%

        % Below this line is the script used to
        % appoximate the vortex ring speed via the
        % images collected from the high speed Schlieren.

        %%%%%
        %%%%%
        %%%%%
        %%%%%

clc
clear
```

```
close all

%%%%%%%%%%%%%%%%%%%%%%%%
% The purpose of this script is to analyze vortex ring
% x(t), VRsize(t), and determine a speed of ring above edge.

% Author: Zachary W. Yoas
% Date: 9/16/2019

%%%%%%%%%%%%%%%%%%%%%%%%%%%%%%%%%%
%% Master Switches
filter_visual = 0; %If 1 then show, if 0 then skip

%%%% What type of case?
%VR or Obstruction
VR_case =1;
Obst_case =0;

%If a VR case do you want to save plot and data?
saveVRdataAndplot =0;

y=47; %set Zp
format short g

%using uiget to obtain a tdms file - assigned path for auto folder
[baseName_data, folder_data]= uigetfile('');

%%%%%%%%%%%%%%%%%%%%%%%%%%%%%%%%%%

%% Obstruction Case
if Obst_case ==1
load_tif_file = strcat(folder_data,baseName_data);
temp = load_tif_file(1:end-28);
```

```
tif_folder_path = (temp); %writing variable for full tif

HSV_frame_rate = 25600; % frame rate on .cine
dirOutput = dir(fullfile(tif_folder_path,'*.tif')); % Locate all .tifs
fileNames = {dirOutput.name}'; %array of all tif file names

VR_Spherical_Shock_Index =input('Enter frame of spherical shock');

if saveVRdataAndplot ==1
temp = strrep(tif_folder_path,'HSV','DAQ'); %swapping drives
temp = temp(1:end-4);% getting rid of run number to produce directory
temp2 = temp(end-2:end); %edits for directory name
temp3 = temp2; %holding onto number
temp2 = str2num(temp2);%edits for directory name
temp2 = sprintf( '%04d', temp2);
%edits for directory name (4 0's instead of 3')
temp = temp(1:end-3);%
temp = strcat(temp,temp2,"\"); %directory name
dir_name = temp;
temp = strcat(temp,"OwlWings",temp3,tif_folder_path(end-3:end));
temp2 = strcat(temp,"_1_VR_data.mat");
VR_char = strcat(temp,"_1_VR_HSV_plot");

%Saving Workspace Data
VR_data = struct();
VR_data.HSV_frame_rate = HSV_frame_rate;
VR_data.VR_Spherical_shock_index = VR_Spherical_Shock_Index;
VR_data.Info = tif_folder_path;
save(temp2,'VR_data')
end
end

%% VR Case
```

```
if VR_case == 1
HSV_obj_cal_distance_cm = 0.64; %Setting the calibration object distance

%% Setting Data Location & Loading Files
load_tif_file = strcat(folder_data,baseName_data);
temp = load_tif_file(1:end-28);
tif_folder_path = (temp); %writing variable for full tif

% Data Read in
HSV_frame_rate = 25600; % frame rate on .cine
dirOutput = dir(fullfile(tif_folder_path,'*.tif')); % Locate all .tifs
fileNames = {dirOutput.name}'; %array of all tif file names
numFrames = numel(fileNames); %total number of images
I = imread(load_tif_file); %loading in sample .tif

%%%%%%%%
% Prepping data for data stepping
VR_image_indexing = 20;
% Setting number of data sections (how many data points)

%If the number of total frames is <20 then use all available,
%else make array for step through images
if numFrames <=20
tot_numFrames_Round = numFrames;
else
temp = linspace(1,numFrames,20);
temp = floor(temp);
step_img = temp;
temp = step_img(end);
end

% Time vector for image step scenarios
for ii = 1:length(step_img)
```

```
if ii == 1
time_vector(ii) = 0;
else
time_vector_image_step(ii) = step_img(ii)/HSV_frame_rate;
end
end

time_vector_image_step = time_vector_image_step.';

% Pre-allocating Arrays
%preallocate 3D matrix
image_sequence = zeros([size(I) numFrames],class(I));

% populate 1st index of image_sequence
image_sequence(:,:,1) = I;

disp('Complete : HSV - Load Files')



% Setting Scale Factor
figure(1)
imshow(load_tif_file)
set(gcf, 'Position', get(0, 'Screensize'));
disp('Click on upper edge of cal object, then bottom edge of cal object')
title('Click on upper edge of cal object, then bottom edge of cal object');
impixelinfo

[xx,yy] = ginput(2);
scale_image(1,1) = xx(1,1);
scale_image(1,2) = xx(2,1);
scale_image(1,3) = yy(1,1);
scale_image(1,4) = yy(2,1);
```

```
%Setting number of pixels correspond to distance
scaling_pixels = yy(2,1)-yy(1,1);
scaling_dist_cm = HSV_obj_cal_distance_cm;

close(1)

%% Finding VR Coordinates from .tifs

if Select_Filter == 1

%Vortex Ring Location (image step size jumps through "x" .tifs)
VR_points = zeros(VR_image_indexing,4);
% col 1 = x1, col 2 = x2, col 3 = y1, col 4 = y2

disp('Select VR top core, then VR bottom core')

% Using crosshairs on image, identifying location VR location

for count_01 = 1:VR_image_indexing

figure(2)
imshow(image_sequence(:,:,(step_img(count_01))));
set(gcf, 'Position', get(0, 'Screensize'));
impixelinfo
title(sprintf('Processed Image # %d',count_01));
set(findobj(gcf,'type','axes'),'FontName','Arial','FontSize',...
12,'FontWeight','Bold', 'LineWidth', 1);
[xx,yy] = ginput(2);

VR_points(count_01,1) = xx(1,1); % Building matrix of X1 Points
VR_points(count_01,2) = xx(2,1); % Building matrix of X2 Points
VR_points(count_01,3) = yy(1,1); % Building matrix of Y1 Points
```

```
VR_points(count_01,4) = yy(2,1); % Building matrix of Y2 Points

VR_avg_X_points(count_01,1) = mean(VR_points(count_01,1:2));
VR_delta_Y_points(count_01,1) = VR_points(count_01,4) -...
VR_points(count_01,3) ;

%Quick indicator for progress
temp_01 = num2str(count_01(1,1));
temp_02 = num2str(VR_image_indexing);

Coordinates_Progress = strcat({'Image Number '},...
temp_01,{' of '},temp_02);
disp(Coordinates_Progress)

end
close (2)
end

if Select_Filter == 2

for count_01 = 1:VR_image_indexing

figure(2)
set(gcf, 'Position', get(0, 'Screensize'));
set(gcf,'units','normalized','outerposition',[0 0 1 1])
imshow(image_sequence_gauss_smooth_contrast(:,:,(count_01*step_img)));
impixelinfo
title(sprintf('Processed Image # %d',step_img*count_01));
set(findobj(gcf,'type','axes'),'FontName','Arial','FontSize',...
12,'FontWeight','Bold', 'LineWidth', 1);
[xx,yy] = ginput(2);

VR_points(count_01,1) = xx(1,1); % Building matrix of X1 Points
```

```
VR_points(count_01,2) = xx(2,1); % Building matrix of X2 Points
VR_points(count_01,3) = yy(1,1); % Building matrix of Y1 Points
VR_points(count_01,4) = yy(2,1); % Building matrix of Y2 Points

VR_avg_X_points(count_01,1) = mean(VR_points(count_01,1:2));
VR_delta_Y_points(count_01,1) = VR_points(count_01,4) -...
VR_points(count_01,3) ;

%Quick indicator for progress
temp_01 = num2str(count_01(1,1));
temp_02 = num2str(VR_image_indexing);

Coordinates_Progress = strcat({'Image Number '},temp_01,...
{' of '},temp_02);
disp('Select VR top core, then VR bottom core')
disp(Coordinates_Progress)

end
close (2)
end

if Select_Filter == 3

for count_01 = 1:VR_image_indexing

figure(2)
set(gcf, 'Position', get(0, 'Screensize'));
set(gcf,'units','normalized','outerposition',[0 0 1 1])
imshow(image_sequence_contrast(:,:,(count_01*step_img)));
impixelinfo
title(sprintf('Processed Image # %d',step_img*count_01));
set(findobj(gcf,'type','axes'),'FontName','Arial','FontSize',...
12,'FontWeight','Bold', 'LineWidth', 1);
```

```
[xx,yy] = ginput(2);

VR_points(count_01,1) = xx(1,1); % Building matrix of X1 Points
VR_points(count_01,2) = xx(2,1); % Building matrix of X2 Points
VR_points(count_01,3) = yy(1,1); % Building matrix of Y1 Points
VR_points(count_01,4) = yy(2,1); % Building matrix of Y2 Points

VR_avg_X_points(count_01,1) = mean(VR_points(count_01,1:2));
VR_delta_Y_points(count_01,1) = VR_points(count_01,4) -...
VR_points(count_01,3) ;


%Quick indicator for progress
temp_01 = num2str(count_01(1,1));
temp_02 = num2str(VR_image_indexing);

Coordinates_Progress = strcat({'Image Number '},temp_01,...
{' of '},temp_02);
disp('Select VR top core, then VR bottom core')
disp(Coordinates_Progress)

end

close (2)
end
disp('Complete : HSV - Extract VR Coordinates')

%% X-position vs time

% Preallocating VR position X location arrays
VR_position_X_mm = zeros(VR_image_indexing,1);

% Vortex X Position (pixel location) to translational distance
```

```
for count_01 = 2:VR_image_indexing
VR_position_X_mm(count_01,1) = VR_avg_X_points(count_01) - ...
VR_avg_X_points(1);
VR_position_X_mm(1,1) = 0;
VR_position_X_mm(count_01,1) = VR_position_X_mm(count_01)*...
(scaling_dist_cm/scaling_pixels)*10;
end


disp('Complete : HSV - X Position vs Time')

%% VR size vs time

% Preallocating VR size array
VR_size_mm = zeros(VR_image_indexing,1);

% Using coordinates to determine the vortex ring size
for count_01 = 1:(VR_image_indexing)
VR_size_mm(count_01,1) = (VR_delta_Y_points(count_01,1))*...
(scaling_dist_cm/scaling_pixels)*10;
end

disp('Complete : HSV - VR Size')


%% User Input VR/Edge Frame Number
VR_Spherical_Shock_Index =input('Enter frame of spherical shock');
VR_Edge_FrameNumber_idx = input('Enter frame number of VR/Edge');

%% Plotting (X vs time & VR size vs time)

% Plotting (X vs time, VR size vs time, VR velocity vs time)
fig_1_xlim_end = (time_vector_image_step(end));
```

```
figure(1)
subplot(1,2,1)
plot(time_vector_image_step(2:end,1),VR_position_X_mm(2:end,1),...
'r*','LineWidth',1.5)
xlabel('Time (sec)','Interpreter','Latex');
ylabel('Flight Distance, ${x_i}$ (mm)','Interpreter','Latex')
grid on
line([0,1],[y,y],'Color','red','LineStyle','--')
xlim([0 fig_1_xlim_end])

% Applying a linear fit to data
ind = find(VR_position_X_mm >(y-6));
%finds start point just beyond edge location
P = polyfit(time_vector_image_step(2:ind(1,1)-1,1),...
VR_position_X_mm(2:ind(1,1)-1,1),1);
yfit = P(1)*(time_vector_image_step(2:ind(1,1)-1,1))+P(2);
hold on
plot(time_vector_image_step(2:ind(1,1)-1,1),yfit,'b-.');
if P(1,2)<0
lin_fit = strcat('y=',num2str(round(P(1,1)/1000,1)),...
'x',num2str(round(P(2),2)));
legend('$x_i (t)$','Edge location',lin_fit,'Location','southeast')
set(legend,'Interpreter','latex')
end

if P(1,2)>0
lin_fit = strcat('y=',num2str(round(P(1,1)/1000,1)),'x+',...
num2str(round(P(2),2)));
legend('$x_i (t)$','Edge location',lin_fit,'Location','southeast')
set(legend,'Interpreter','latex')
end

```

```
%finding slope at 2 points by edge
Y2 = (P(1)*(time_vector_image_step(ind(2,1),1))+P(2));
Y1 = (P(1)*(time_vector_image_step(ind(1,1),1))+P(2));
X2 = time_vector_image_step(ind(2,1),1);
X1 = time_vector_image_step(ind(1,1),1);
ring_speed = ((Y2-Y1)/(X2-X1))/1000;
%Since ring_speed is in cm need to convert to m/s

temp=strcat('Ring speed 6mm before edge =','{ }',...
num2str(round(ring_speed,1)),'{ }','m/s');
title(temp,'Interpreter','Latex')


% Plotting Ring Size
subplot(1,2,2)
plot(time_vector_image_step(2:end,1),VR_size_mm(2:end,1),...
'r*','LineWidth',1.5)
xlabel('Time (sec)','Interpreter','Latex');
ylabel('Vortex Ring Diameter, ${d_r}$ (mm)','Interpreter','Latex')
grid on
xlim([0 fig_1_xlim_end])
ylim([0 max(VR_size_mm)+4])
end
```

Bibliography

[1] Chen, H. and J. Jaworski (2020) "Noise generation by a vortex ring near porous and elastic edges," in AIAA AVIATION 2020 FORUM, p. 2526.

[2] Williams, J. F. and L. Hall (1970) "Aerodynamic sound generation by turbulent flow in the vicinity of a scattering half plane," Journal of fluid mechanics, **40**(4), pp. 657–670.

[3] Papamoschou, D. (2004) "New method for jet noise reduction in turbofan engines," AIAA journal, **42**(11), pp. 2245–2253.

[4] Oerlemans, S., M. Fisher, T. Maeder, and K. Kögler (2009) "Reduction of wind turbine noise using optimized airfoils and trailing-edge serrations," AIAA journal, **47**(6), pp. 1470–1481.

[5] Kuehnelt, H., A. Zanon, M. Gennaro, D. Langmayr, and D. Caridi (2014) "„Reliable CFD/CAA broadband noise prediction of an unducted low speed axial HVAC fan "," Proceedings of ISMA2014 including USD2014, p. 5.

[6] Sinibaldi, G. and L. Marino (2013) "Experimental analysis on the noise of propellers for small UAV," Applied Acoustics, **74**(1), pp. 79–88.

[7] Arnett, E. B. and R. F. May (2016) "Mitigating wind energy impacts on wildlife: approaches for multiple taxa," Human–Wildlife Interactions, **10**(1), p. 5.

[8] Bolin, K., G. Bluhm, G. Eriksson, and M. E. Nilsson (2011) "Infrasound and low frequency noise from wind turbines: exposure and health effects," Environmental research letters, **6**(3), p. 035103.

[9] Hayden, R. E. (1972) "Noise from interaction of flow with rigid surfaces: a review of current status of prediction techniques," .

[10] Goldstein, M. E. (1976) "Aeroacoustics," New York.

[11] Kambe, T., T. Minota, and Y. Ikushima (1985) "Acoustic wave emitted by a vortex ring passing near the edge of a half-plane," Journal of Fluid Mechanics, **155**, pp. 77–103.

[12] Fink, M. R. (1975) "Experimental evaluation of theories for trailing edge and incidence fluctuation noise," AIAA Journal, **13**(11), pp. 1472–1477.

[13] Brooks, T. F. and T. Hodgson (1981) "Trailing edge noise prediction from measured surface pressures," Journal of sound and vibration, **78**(1), pp. 69–117.

[14] Oerlemans, S. and P. Migliore (2004) "Wind tunnel aeroacoustic tests of six airfoils for use on small wind turbines," Report of the National Renewable Energy Laboratory NREL/SR-500-35339.

[15] Geyer, T., E. Sarradj, and C. Fritzsche (2010) "Measurement of the noise generation at the trailing edge of porous airfoils," Experiments in fluids, **48**(2), pp. 291–308.

[16] Herr, M. and J. Reichenberger (2011) "In search of airworthy trailing-edge noise reduction means," in 17th AIAA/CEAS Aeroacoustics Conference (32nd AIAA Aeroacoustics Conference), p. 2780.

[17] Graham, R. (1934) "The silent flight of owls," The Aeronautical Journal, **38**(286), pp. 837–843.

[18] Kroeger, R. A., H. D. Grushka, and T. C. Helvey (1972) Low speed aerodynamics for ultra-quiet flight, Tech. rep., TENNESSEE UNIV SPACE INST TULLAHOMA.

[19] Klan, S., T. Bachmann, M. Klaas, H. Wagner, and W. Schröder (2010) "Experimental analysis of the flow field over a novel owl based airfoil," in Animal Locomotion, Springer, pp. 413–427.

[20] Bachmann, T. (2010) "Anatomical, morphometrical and biomechanical studies of barn owls' and pigeons' wings," RWTH Aachen University, Germany (PhD thesis).

[21] Lilley, G. (1998) "A study of the silent flight of the owl," in 4th AIAA/CEAS aeroacoustics conference, p. 2340.

[22] Sarradj, E., C. Fritzsche, and T. Geyer (2011) "Silent owl flight: bird flyover noise measurements," AIAA journal, **49**(4), pp. 769–779.

[23] Geyer, T., E. Sarradj, and C. Fritzsche (2012) "Silent owl flight: acoustic wind tunnel measurements on prepared wings," in 18th AIAA/CEAS Aeroacoustics Conference (33rd AIAA Aeroacoustics Conference), p. 2230.

[24] Geyer, T. F. and E. Sarradj (2014) "Trailing edge noise of partially porous airfoils," in 20th AIAA/CEAS Aeroacoustics Conference, p. 3039.

[25] Clark, I. A. (2017) Bio-inspired control of roughness and trailing edge noise, Ph.D. thesis, Virginia Tech.

[26] Clark, I., D. Baker, W. N. Alexander, W. J. Devenport, S. A. Glegg, J. Jaworski, and N. Peake (2016) "Experimental and theoretical analysis of bio-inspired trailing edge noise control devices," in 22nd AIAA/CEAS Aeroacoustics Conference, p. 3020.

[27] Clark, I. A., W. N. Alexander, W. Devenport, S. Glegg, J. W. Jaworski, C. Daly, and N. Peake (2017) "Bioinspired trailing-edge noise control," AIAA Journal, **55**(3), pp. 740–754.

[28] Leppington, F. (1977) "The effective compliance of perforated screens," Mathematika, **24**(2), pp. 199–215.

[29] Leppington, F. G. (1990) "The effective boundary conditions for a perforated elastic sandwich panel in a compressible fluid," Proceedings of the Royal Society of London. A. Mathematical and Physical Sciences, **427**(1873), pp. 385–399.

[30] Howe, M. S. (1978) "A review of the theory of trailing edge noise," Journal of sound and vibration, **61**(3), pp. 437–465.

[31] Howe, M. S. and M. S. Howe (1998) Acoustics of fluid-structure interactions, Cambridge university press.

[32] Khorrami, M. R. and M. M. Choudhari (2003) "Application of passive porous treatment to slat trailing edge noise," .

[33] Jaworski, J. W. and N. Peake (2013) "Aerodynamic noise from a poroelastic edge with implications for the silent flight of owls," Journal of Fluid Mechanics, **723**, pp. 456–479.

[34] Cavalieri, A., W. Wolf, and J. Jaworski (2016) "Numerical solution of acoustic scattering by finite perforated elastic plates," Proceedings of the Royal Society A: Mathematical, Physical and Engineering Sciences, **472**(2188), p. 20150767.

[35] Zhou, B. Y., S. R. Koh, N. R. Gauger, M. Meinke, and W. Schöder (2018) "A discrete adjoint framework for trailing-edge noise minimization via porous material," Computers & Fluids, **172**, pp. 97–108.

[36] Kisil, A. and L. J. Ayton (2018) "Aerodynamic noise from rigid trailing edges with finite porous extensions," Journal of Fluid Mechanics, **836**, pp. 117–144.

[37] Hromisin, S. M., D. K. McLaughlin, and P. J. Morris (2019) "Effects of nozzle configuration and bypass ratio on the aeroacoustics of dual stream supersonic jets," in 25th AIAA/CEAS Aeroacoustics Conference, 2019, American Institute of Aeronautics and Astronautics Inc, AIAA.

[38] McPhail, M. J., E. T. Campo, and M. H. Krane (2019) "Aeroacoustic source characterization in a physical model of phonation," The Journal of the Acoustical Society of America, **146**(2), pp. 1230–1238.

[39] Lighthill, M. J. (1952) "On sound generated aerodynamically I. General theory," Proceedings of the Royal Society of London. Series A. Mathematical and Physical Sciences, **211**(1107), pp. 564–587.

[40] Powell, A. (1964) "Theory of vortex sound," The journal of the acoustical society of America, **36**(1), pp. 177–195.

[41] Möhring, W. (1978) "On vortex sound at low Mach number," Journal of Fluid Mechanics, **85**(4), pp. 685–691.

[42] Obermeier, F. (1980) "The influence of solid bodies on low Mach number vortex sound," Journal of Sound and Vibration, **72**(1), pp. 39–49.

[43] Kambe, T. and T. Minota (1981) "Sound radiation from vortex systems," Journal of Sound and Vibration, **74**(1), pp. 61–72.

[44] Kambe (1983) "Acoustic wave radiated by head-on collision of wo vortex rings," Proceedings of the Royal Society of London. A. Mathematical nd Physical Sciences, **386**(1791), pp. 277–308.

[45] Curle, N. (1956) "Unsteady two-dimensional flows with free boundaries.-I. General theory," Proceedings of the Royal Society of London. Series A. Mathematical and Physical Sciences, **235**(1202), pp. 375–381.

[46] Luong, T., M. S. Howe, and R. S. McGowan (2005) "On the Rayleigh conductivity of a bias-flow aperture," Journal of Fluids and Structures, **21**(8), pp. 769–778.

[47] Jaworski, J. W. and N. Peake (2020) "Aeroacoustics of silent owl flight," Annual Review of Fluid Mechanics, **52**, pp. 395–420.